Wavelet-based wavenumber spectral estimate of eddy kinetic energy: Application to the North Atlantic

Takaya Uchida, FSU (tuchida@fsu.edu)
Quentin Jamet, INRIA (quentin.jamet@inria.fr)
Andrew C. Poje, CUNY (andrewpoje@gmail.com)
Nico Wienders (nwienders@fsu.edu)
William K. Dewar, FSU (wdewar@fsu.edu)

Highlights

Wavelet-based wavenumber spectral estimate of eddy kinetic energy: Application to the North Atlantic

Takaya Uchida, Quentin Jamet, Andrew C. Poje, Nico Wienders, William K. Dewar

- Eddies are defined as fluctuations about an ensemble mean for the North Atlantic.
- Wavelet transform is used to estimate the wavenumber spectra and spectral flux.
- The wavelet method is consistent with Fourier and can close the spectral budget.
- We are able to extract the spatial anisotropy and time dependence of eddies.
- Our wavelet algorithm scales as computing the continuous Fourier transform.

Wavelet-based wavenumber spectral estimate of eddy kinetic energy: Application to the North Atlantic

Takaya Uchida[a,b,*], Quentin Jamet[c,d], Andrew C. Poje[e], Nico Wienders[a], William K. Dewar[b,f]

[a] *Center for Ocean-Atmospheric Prediction Studies, Florida State University, Tallahassee, Florida, USA*
[b] *Université Grenoble Alpes, CNRS, INRAE, IRD, Grenoble INP, Institut des Géosciences de l'Environnement, Grenoble, France*
[c] *Institut National de Recherche en Sciences et Technologies du Numérique (INRIA), Ocean DYnamicS obSErvation analYsis (ODYSSEY), Ifremer, Plouzané, France*
[d] *Service Hydrographique et Océanographique de la Marine (SHOM), Brest, France*
[e] *Department of Mathematics, College of Staten Island, The City University of New York, NYC, New York, USA*
[f] *Department of Earth, Ocean and Atmospheric Science, Florida State University, Tallahassee, Florida, USA*

Abstract

An ensemble of eddy-rich North Atlantic simulations is analyzed, providing estimates of eddy kinetic energy (EKE) wavenumber spectra and spectral budgets below the mixed layer where energy input from surface convection is negligible. A wavelet transform technique is used to estimate a spatially localized 'pseudo-Fourier' spectrum, permitting comparisons to be made between spectra at different locations in a highly inhomogeneous and anisotropic environment (Uchida et al., 2023b). The EKE spectra tend to be stable in time but the spectral budgets are highly time dependent. We find evidence of a Gulf Stream imprint on the near Gulf Stream eddy field appearing as enhanced levels of EKE in the (nominally) North-South direction relative to the East-West direction. Surprisingly, this signature of anisotropy holds into the quiescent interior with a tendency of the orientation aligned with maximum EKE being associated with shallower spectral slopes and elevated levels of inverse EKE cascade. Conversely, the angle associated with minimum EKE is aligned with a steeper spectral slope and forward cascade of EKE. A summary conclusion is that the spectral characteristics of eddies in the wind-driven gyre below the mixed layer where submesoscale and frontal dynamics are expected to be weak tend to diverge from expectations built on inertial-range assumptions, which are stationary in time and horizontally isotropic in space.

Keywords: Wind-driven gyre, Ensemble simulation, Mesoscale eddies, Wavenumber spectra, Spectral budget, Wavelets

1. Introduction

The ocean is 'turbulent', implying the presence of energetic and widespread spatial and temporal 'eddies' (Stammer, 1998; Stammer and Wunsch, 1999). It is now commonly ac-

*Email: tuchida@fsu.edu. Will be moving to the *Climate Dynamics Lab, МФТИ.*

cepted in ocean modeling that resolving these features, at least at the mesoscale, leads to ocean simulations of a much more realistic nature (Chassignet and Marshall, 2008; Chassignet et al., 2020, 2023; Griffies et al., 2015; Uchida et al., 2020; Constantinou and Hogg, 2021; Xu et al., 2022), which may have important implications for climate projections (Saba et al., 2016; Beech et al., 2022). This implies the eddy field is an integral part of the ocean structure, and a necessary feature to either implicitly or explicitly include within the ocean component of any climate model. The computational demands of eddy-resolving resolution have led to the search for eddy parameterizations that faithfully capture the dynamical role of eddies in the absence of their explicit presence (e.g. Redi, 1982; Gent and McWilliams, 1990; Gent, 2011; Jansen et al., 2019; Guillaumin and Zanna, 2021; Berloff et al., 2021; Uchida et al., 2022a; Li et al., 2023; Deremble et al., 2023, and references therein). It is essential therefore to understand the behavior of the eddy field in well-resolved models in order to ascertain the character eddy parameterizations should portray and to provide benchmarks for assessing the affects of any particular proposed parameterization. This paper attempts to serve these purposes by describing and applying a methodology that allows for spatial inhomogeneity in the mean flow to influence eddy characteristics. We analyze a recently developed ensemble of North Atlantic simulations (Jamet et al., 2019a,b) and use two-dimensional wavelet analysis to diagnose the spectral structure.

Most available theoretical guidance on oceanic turbulence comes from quasi-geostrophic (QG) theory, where the combined conservations of energy and potential vorticity (PV) lead to predictions for specific shapes for wavenumber spectra. Surface quasi geostrophy (SQG), on the other hand, employs conservation of surface buoyancy instead of PV (Held et al., 1995; Lapeyre, 2017; Yassin and Griffies, 2022). It is generally thought that the eddy field should display a so-called '$-5/3$' spectral slope as a result of an up-scale cascade of energy, and a '-3' slope due to a down-scale enstrophy cascade (Charney, 1971). Both predictions are based on the ideas of inertial ranges and involve a reasonable number of assumptions. Locality in spectral interactions, stationarity in time and homogeneity in space are amongst the most prominent assumptions; a thorough discussion appears in Vallis (2006). Numerical, observational and laboratory investigations in relevant settings tend to support the predictions (e.g. Gage and Nastrom, 1986; Yarom et al., 2013; Callies and Ferrari, 2013; Campagne et al., 2014).

The inertial-range ideas are usually adopted when venturing into the more dynamically complex settings of primitive equations and realistic ocean simulations (e.g. Xu and Fu, 2011, 2012; Khatri et al., 2018; Vergara et al., 2019), although it is difficult to justify many of the assumptions. In particular, as will often be the focus of this paper, the presence of the Gulf Stream would seem to violate spatial homogeneity in the field in which the eddies are viewed. In addition, and perhaps at an even more fundamental level, the mix of a coherent, large-scale mean with an incoherent, variable component renders the definition of what constitutes an 'eddy' somewhat vague. One then questions what features should be focused on when constructing a spectrum (cf. Uchida et al., 2021c). This problem of identifying or defining ocean eddies is a well known one, with an early reference being Wunsch (1981).

Another problem facing the quantification of the eddy field in an inhomogeneous setting is a lack of available techniques for analyzing the data. A favorite, and classical, method for studying wavenumber spectra employs Fourier transforming momentum (e.g. Capet et al., 2008; Callies and Ferrari, 2013; Rocha et al., 2016; Uchida et al., 2017, 2019; Ajayi et al., 2020; Khatri et al., 2018, 2021). The connection between this measure and kinetic energy (KE) comes from Parseval's theorem, which equates the area integrated KE to the wavenumber integrated spectrum

$$\int_{\boldsymbol{x}} |\boldsymbol{u}(\boldsymbol{x})|^2 \,\mathrm{d}\boldsymbol{x} = \int_{\boldsymbol{k}} \hat{\boldsymbol{u}} \cdot \hat{\boldsymbol{u}}^* \,\mathrm{d}\boldsymbol{k} \tag{1}$$

where $\hat{\boldsymbol{u}}$ is the Fourier transform of $\boldsymbol{u} \overset{\text{def}}{=} u\boldsymbol{e}_1 + v\boldsymbol{e}_2$, the horizontal velocity, and $\boldsymbol{e}_1$ and $\boldsymbol{e}_2$ are the zonal and meridional unit vector respectively. This permits the interpretation of the spectrum in terms of a wavenumber dependent energy density. However, this same equivalence then implies the resultant spectra are averages over the domain involved in the analysis. While this does not represent a conceptual problem if the domain is spatially homogeneous, the relation of the result to the local spectrum in an inhomogeneous setting is not clear. Such shortcomings have been identified by the community and have motivated the development of other approaches, e.g. structure functions (Poje et al., 2017; Pearson et al., 2020; Balwada et al., 2022) and spatial coarse graining (Aluie et al., 2018; Sadek and Aluie, 2018; Zhao et al., 2022).

Our primary numerical tool to tackle these questions is a recently developed eddying 48-member ensemble of partially air-sea coupled North Atlantic simulations. These simulations have been used before in studies of North Atlantic energetics (Jamet et al., 2020b; Uchida et al., 2024), the Atlantic Meridional Overturning Circulation (AMOC; Jamet et al., 2019b, 2020c; Dewar et al., 2022), Empirical Orthogonal Function (EOF) analyses of eddies (Uchida et al., 2021c), and the thickness-weighted averaged (TWA) feedback of eddies on the residual-mean flow (Uchida et al., 2022b, 2023a). A full description of the simulations appears in Jamet et al. (2019b). For our purposes, the ensemble consists of 48 members exposed to *small* initial-condition uncertainties (usually referred to as *micro* initial conditions; Stainforth et al., 2007) run at an 'eddy-rich' 1/12° resolution. A map of the surface local Rossby number appears in Fig. 1, displaying the expected activity around the Gulf Stream region, with a separation from the coastal U.S. around Cape Hatteras, and extension into the North Atlantic Current. Also shown are two marked locations A and B, which will be referred to later in the text as dynamically distinct locations within the wind-driven gyre as implied from the magnitude in local Rossby numbers.

We assert that such an ensemble leads to a clear identification of oceanic eddies, namely as fluctuations about the ensemble mean. Specifically, we can average our simulations at any space and time point across our ensembles to obtain an estimate of the classical ensemble mean. Then, we can revisit each individual ensemble member to compute its deviation from the ensemble mean at that same spatial and temporal location. Inasmuch as the ensemble mean represents that component of the solution common to all members, we identify it as the predictable part of the flow. The residuals, belonging to each individual realization, are the 'unpredictable' components of the flow and are identified as the eddies. An attempt to rationalise this in terms of integrated KE budgets has recently been proposed by Jamet

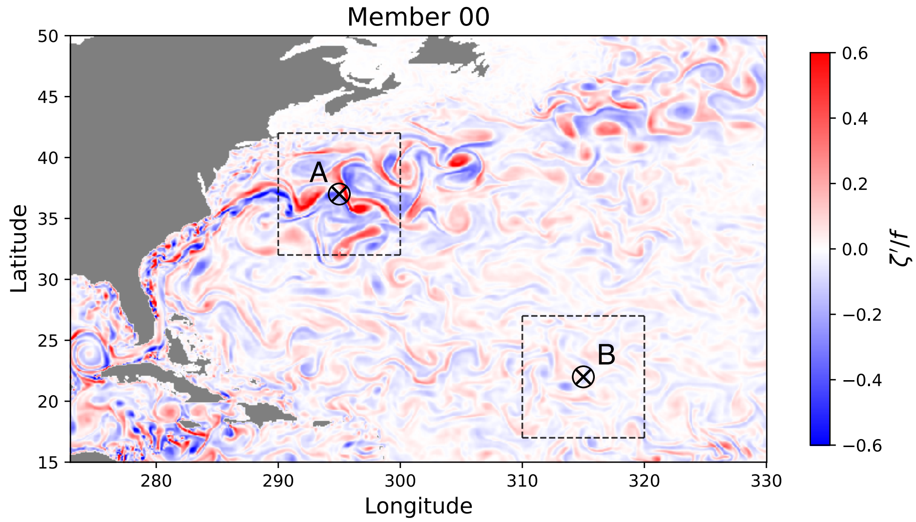

Figure 1: Surface eddy relative vorticity from member 00 amongst the 48 ensemble members at 00:10, January 1, 1967 normalized by the local Coriolis frequency. Land and coastlines are in grey; the Gulf Stream and its extension into the open Atlantic are visible. Location A within the Gulf Stream near to separation at Cape Hatteras is marked, as is location B in the North Atlantic. These locations will be referred to later in the text. The dashed lines indicate the $10^\circ \times 10^\circ$ domains over which the wavelet and Fourier transforms are applied.

et al. (2022). Note that this eddy definition is independent of any arbitrarily chosen spatial or temporal scale, a highly desirable feature not characteristic of most definitions reliant on some form of spatial or temporal filtering (Chen and Flierl, 2015; Uchida et al., 2021a,c; Berloff et al., 2021). These eddies are the ones we propose to quantify.

As to spectral computations, we proceed using a wavelet-based analysis. To our knowledge, the wavelet approach to wavenumber spectra was initially examined by Daubechies (1992) and Perrier et al. (1995) and in an oceanographic context by Uchida et al. (2023b). For our purposes, we will interpret the spectra computed using wavelets as an estimate of a *localized* 'pseudo-Fourier' spectrum, which is backed by Parseval's equality (Uchida et al., 2023b). The spatial locality of these estimates permits us to examine and compare the variability of spectra throughout the domain.

Our eddy definition is reviewed briefly in the next section, along with a description of our wavelet-based analysis methods. Section 3 presents a comparison between wavelet-based spectral estimates and the canonical Fourier-based estimates within the North Atlantic gyre. The paper ends with a Discussion, speculations on the relevant dynamics and plans for further work.

2. Theory and techniques

In this section, we describe our definition of 'eddies' (Section 2.1) and provide an overview on wavelet spectral analysis (Section 2.2).

2.1. Eddy Definition

Due to the chaotic nature of the ocean (Poincaré, 1890; Lorenz, 1963), trajectories of eddying numerical simulations are sensitive to initial condition uncertainties (e.g. Kay et al., 2015; Sérazin et al., 2017; Maher et al., 2019; Zhao et al., 2021; Uchida et al., 2021b; Leroux et al., 2018, 2022; Jamet et al., 2022; Germe et al., 2022; Romanou et al., 2023). This allows us to develop an ensemble of ocean simulations, differing only in small ways in their initial conditions; i.e. simulations based on initial states that have small differences well within current measurement uncertainties. It is a matter of experience that while gross characteristics of the resulting fully evolved states are similar (there will always be a Gulf Stream, for example), the mesoscale fields become incoherent. While each ensemble solution represents an equally valid and plausible simulation of the North Atlantic, none of them at any specified date will recreate the observed ocean state since the observed ocean is itself a single realization of the chaotic system.

From such an ensemble, one can take an 'ensemble mean', which we will denote by brackets, i.e. for any model variable $\psi(\boldsymbol{x}, t)$,

$$\langle \psi(\boldsymbol{x}, t) \rangle = \frac{1}{N} \sum_{i=1}^{N} \psi^i(\boldsymbol{x}, t)\,, \tag{2}$$

where $N(= 48)$ is the total number of ensemble members and the superscript i denotes the ensemble member. We interpret the ensemble mean as the 'forced' response of the ocean. That is, as the ensemble mean is common to all members, it reflects the common external conditions imposed at the boundaries of the system. In our case, these common conditions consist of the prescribed atmospheric states and the open ocean boundary conditions at the northern and southern domain boundaries and the Strait of Gibraltor (Jamet et al., 2019b).

The eddy field is denoted by deviations of ψ about the ensemble mean

$$\psi^{i\prime}(\boldsymbol{x}, t) = \psi^i(\boldsymbol{x}, t) - \langle \psi(\boldsymbol{x}, t) \rangle\,. \tag{3}$$

Each member, i, having its own eddy field thus identifies the eddies as an unpredictable component of the flow. Note that the ensemble mean in (2) is inherently a function of space and time, a feature which permits the examination of the non-stationary and inhomogeneous character of the statistics. It is a strength of the ensemble dimension, being orthogonal to the space-time dimensions, that these features of non-stationarity and inhomogeneity are preserved.

Finally, we note that the ensemble mean structure of the ocean is not independent of the eddies, rather the non-linear equations of motion for the ensemble mean involve second-order measures of the eddies as part of their balance. Fluctuations about the mean in any realization are, in turn, constrained by the lower-order statistics of the mean and eddy contributions.

2.2. Spectral Considerations

We depart from the classical Fourier approach to compute wavenumber spectra for our non-periodic and inhomogenous settings, noting that the utility of wavenumber spectrum emerges largely from Parseval's equality. We base our spectral analysis on wavelet decompositions. Here, we provide a brief overview.

Given a function of two spatial dimensions, $f(\boldsymbol{x})$, its continuous wavelet transform is given by

$$\tilde{f}(s,\phi,\boldsymbol{\gamma}) = \int_{\boldsymbol{x}} f(\boldsymbol{x})\frac{1}{s}\xi^*(\mathbf{R}^{-1}\cdot\left(\frac{\boldsymbol{x}-\boldsymbol{\gamma}}{s}\right))\,\mathrm{d}\boldsymbol{x}\,, \tag{4}$$

where $\mathbf{R}^{-1}$ is the inverse of the rotation matrix

$$\mathbf{R}^{-1} = \begin{pmatrix} \cos(\phi) & \sin(\phi) \\ -\sin(\phi) & \cos(\phi) \end{pmatrix}\,, \tag{5}$$

for rotation through an angle ϕ. The quantity s is referred to as the 'scale', $\boldsymbol{\gamma}\,(\in\mathbb{R}^2)$ is the two-dimensional coordinates of interest, $\xi(\boldsymbol{x})$ is the so-called 'mother' wavelet and $\xi(\mathbf{R}^{-1}\cdot(\boldsymbol{x}-\boldsymbol{\gamma})/s)$ in (4) are the daughter wavelets. The quantities $\tilde{f}$ are the wavelet coefficients. Subject to a few, relatively easy to meet conditions (Uchida et al., 2023b), the original data can be reconstructed from the wavelet coefficients via an inverse wavelet transform

$$f(\boldsymbol{x}) = \mathscr{C}\int_{\boldsymbol{\gamma}}\int_{\phi}\int_{s}\frac{1}{s^4}\tilde{f}(s,\phi,\boldsymbol{\gamma})\xi(\mathbf{R}^{-1}\cdot\left(\frac{\boldsymbol{x}-\boldsymbol{\gamma}}{s}\right))\,\mathrm{d}s\,\mathrm{d}\phi\,\mathrm{d}\boldsymbol{\gamma} \tag{6}$$

where $\mathscr{C}$ is a constant, to be clarified below. Exploiting the properties of wavelets, it is possible to show they satisfy a generalized Parseval's equality

$$\int_{\boldsymbol{x}} f(\boldsymbol{x})g(\boldsymbol{x})\,\mathrm{d}\boldsymbol{x} = \mathscr{C}\int_{\boldsymbol{\gamma}}\int_{\phi}\int_{s}\frac{\tilde{f}\tilde{g}^*}{s^3}\,\mathrm{d}s\,\mathrm{d}\phi\,\mathrm{d}\boldsymbol{\gamma}, \tag{7}$$

with $(\cdot)^*$ the complex conjugate. Note, if $f=g$, (7) corresponds to the Parseval's equality in (1).

We employ the so-called Morlet wavelet (Morlet et al., 1982; Gabor, 1946), i.e.

$$\xi(\boldsymbol{x}) = \left(e^{-2\pi i\boldsymbol{k}_0\cdot\boldsymbol{x}} - c_0\right)e^{-\frac{\boldsymbol{x}\cdot\boldsymbol{x}}{2x_0^2}}\,, \tag{8}$$

where c_0 is a constant included to insure that the wavelet has zero mean $\int_{\boldsymbol{x}}\xi(\boldsymbol{x})\,\mathrm{d}\boldsymbol{x} = 0$. The central wavenumber $\boldsymbol{k}_0$ is taken to be $\boldsymbol{k}_0 = (k_0, 0)$ and the quantity x_0 is a reference length scale, here taken to be 50 km, viz. the length scale of the mother wavelet. The zonal orientation of wavevector $\boldsymbol{k}_0$ is arbitrary as we will rotate the orientation with $\mathbf{R}$. We will choose $k_0 = 1/x_0$, in which case the constant c_0 is quite small and generally ignored (i.e. $c_0 = 0$), a convention adopted in this paper. Plots of (8) are found in Fig. 2. Note that the Morlet mother wavelet consists of a wave of wavelength $L = x_0$ inside a Gaussian envelope of decay scale $\sqrt{2}x_0$. Thus for $s = 1$ and $\phi = 0$, the wavelet coefficient produced by this transformation comments on the presence of the wavenumber $\boldsymbol{k}_0 = (k_0, 0)$ at location $\boldsymbol{\gamma}$ in the original data. Increasing the rotation angle ϕ and filtering returns information about the presence of the same wavelength at angle ϕ. Finally allowing s to vary modifies the filter so that the primary wavelength of the filter is $k = 1/(sx_0)$. The Morlet wavelet coefficient

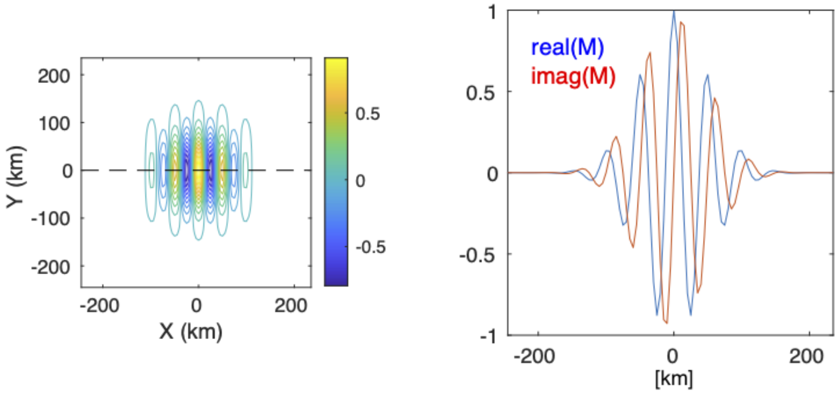

Figure 2: Structure of the Morlet wavelet with the reference length scale $x_0 = 50\,\mathrm{km}$. A contour plot of the real part of the mother Morlet wavelet is shown in the left panel. Transects of the real and imaginary parts along the dashed line appear in the right panel.

can thus be thought of as a spatially 'local' Fourier transform at wavenumber $\boldsymbol{k}_0^{\mathsf{T}} \cdot \mathsf{R}^{-1}(\phi)/s$, where the superscript T denotes a transpose.

At this point, the scale factor in (4), s, is non-dimensional. It is more traditional in oceanography to discuss energy spectra in terms of wavenumber. As pointed out above, the effective wavenumber associated with s is $k = 1/(sx_0) = 1/s_0$, where the quantity s_0 has units of length. Upon some algebra, one may transform (7) (with $f = g$) to wavenumber, $k = 1/s_0$, space, ending with

$$\int_{\boldsymbol{x}} f^2(\boldsymbol{x})\,\mathrm{d}\boldsymbol{x} = \frac{1}{C_\Xi} \int_\phi \int_k \int_{\boldsymbol{\gamma}} \tilde{f}^* \tilde{f} k x_0^2 \,\mathrm{d}\boldsymbol{\gamma}\,\mathrm{d}k\,\mathrm{d}\phi\,, \tag{9}$$

where $C_\Xi = \int_{\boldsymbol{k}} \frac{\hat{\Xi}^* \hat{\Xi}}{\boldsymbol{k}\cdot\boldsymbol{k}}\,\mathrm{d}\boldsymbol{k}$ and $\hat{\Xi}$ is the Fourier transform of the mother wavelet (cf. Uchida et al., 2023b). Note, $\mathscr{C} = C_\Xi^{-1}$ in (7).

If we now produce wavelet coefficients for the zonal and meridional eddy velocities u'^i and v'^i from member i of our ensemble, and manipulate them appropriately, we obtain

$$\mathscr{K}_K^i(\boldsymbol{\gamma}, \phi, k) = \frac{1}{C_\Xi} \frac{\tilde{u'^i}\tilde{u'^i}^* + \tilde{v'^i}\tilde{v'^i}^*}{2} x_0^2 k\,, \tag{10}$$

as a measure of energy density in wavelet transform space. Each value of $\mathscr{K}_K^i$ is a random number as each ensemble member possesses a 'random' eddy field emerging from the non-linearities in the system. Ensemble averaging those values returns an estimate of the ensemble-mean energy spectrum as a function of wavenumber k in direction ϕ. The spatial locality of the mother wavelet permits the interpretation of $\mathscr{K}_K(s, \phi, \boldsymbol{\gamma}) = \langle \mathscr{K}_K^i(s, \phi, \boldsymbol{\gamma}) \rangle$ as the local energy spectrum at location $\boldsymbol{\gamma}$ (Table 1).

In calculating the wavelet coefficients, we spatially interpolate each $10° \times 10°$ domain centered around each $\otimes$ in Fig. 1 onto a uniform grid (cf. Section 3). The wavelet transform appropriate to the scale factor s was then taken between $[k_F^{\min}, k_F^{\max}]$ with 40 monotonic increments where $k_F^{\min}$ and $k_F^{\max}$ are the minimum and maximum Fourier wavenumbers respectively leaving us with 47 increments, and angle ϕ with the resolution of $\pi/18$ radian $(= 10°)$

between $[0, \pi)$. The scaling was then truncated at scales below 50 km and appended with scales corresponding to the Fourier wavenumbers to increase the wavenumber resolution at higher wavenumbers. The spatial integration of the product of the wavelet and the data is the wavelet coefficient for each location. The computational cost of our wavelet transform Python package (Uchida and Dewar, 2022) scales as one would take the continuous Fourier transform, i.e. $\mathcal{O}(n^2)$ unlike $\mathcal{O}(n \ln n)$ as in fast Fourier transform (FFT) algorithms where n is the size of data (Uchida et al., 2021d).

Table 1: Notation of the variables and description. The definition for the spectral budget terms is given in Appendix A. $\mathcal{R}[\cdot]$ indicates the real part.

Mathematical notation	Description
$K = \frac{1}{2}\lvert\boldsymbol{u}\rvert^2$	Total kinetic energy (TKE)
$K^{\#} = \frac{1}{2}\lvert\langle\boldsymbol{u}\rangle\rvert^2$	Mean kinetic energy (MKE)
$\langle\mathscr{K}\rangle = \frac{1}{2}\langle\lvert\boldsymbol{u}'\rvert^2\rangle$	Eddy kinetic energy (EKE)
$\mathscr{K}_K = \frac{1}{2C_\Xi}\left\langle \widetilde{u'}^*\widetilde{u'} + \widetilde{v'}^*\widetilde{v'}\right\rangle x_0^2 k$	EKE spectrum
$\mathcal{T}_K = \frac{1}{C_\Xi}\mathcal{R}\left[\langle\widetilde{\boldsymbol{u}'}^*\cdot\widetilde{\boldsymbol{u}'_t}\rangle\right] x_0^2 k$	Spectral tendency of EKE
$\mathcal{P}_K = -\frac{1}{C_\Xi}\mathcal{R}\left[\langle\widetilde{\boldsymbol{u}'}^*\cdot\widetilde{\nabla_{\mathrm{h}}\phi'}\rangle\right] x_0^2 k$	Spectral pressure work to EKE
$\begin{aligned}\mathcal{A}_K &= -\frac{1}{C_\Xi}\mathcal{R}\Big[\langle\widetilde{u'}^*(\widetilde{\boldsymbol{v}\cdot\nabla u'})\rangle + \langle\widetilde{v'}^*(\widetilde{\boldsymbol{v}\cdot\nabla v'})\rangle\Big]x_0^2 k \\ &= -\frac{1}{C_\Xi}\mathcal{R}\Big[\Big\langle\widetilde{u'}^*\widetilde{(\boldsymbol{v}\cdot\nabla u)'}\Big\rangle + \Big\langle\widetilde{v'}^*\widetilde{(\boldsymbol{v}\cdot\nabla v)'}\Big\rangle - \Big\langle\widetilde{u'}^*\widetilde{\boldsymbol{v}'\cdot\nabla\langle u\rangle}\Big\rangle - \Big\langle\widetilde{v'}^*\widetilde{\boldsymbol{v}'\cdot\nabla\langle v\rangle}\Big\rangle\Big]x_0^2 k\end{aligned}$	Spectral transfer of EKE
$\mathcal{D}_K = \frac{1}{C_\Xi}\mathcal{R}\left[\langle\widetilde{\boldsymbol{u}'}^*\cdot\widetilde{\boldsymbol{\mathcal{X}}'}\rangle\right] x_0^2 k$	Spectral diabatic terms of EKE
$\mathrm{MtE}_K = -\frac{1}{C_\Xi}\mathcal{R}\left[\Big\langle\widetilde{u'}^*\widetilde{\boldsymbol{v}'\cdot\nabla\langle u\rangle}\Big\rangle - \Big\langle\widetilde{v'}^*\widetilde{\boldsymbol{v}'\cdot\nabla\langle v\rangle}\Big\rangle\right] x_0^2 k$	Spectral shear production
$\varepsilon_K(k) = \int_{k>\kappa}\mathcal{A}_K(\kappa)\,\mathrm{d}\kappa$	Spectral flux of EKE

3. Results

In this section, we examine the kinetic energy (KE) and spectral flux from the two locations in Fig. 1 at the surface and below the mixed layer ($z = -3$, -452 m respectively). The depth of 452 m was chosen to be within the general wind-driven circulation but well beneath the mixed layer in order to avoid KE input from convective events (cf. Uchida et al., 2022b, their Fig. 2b), in our case parametrized by the K-profile parametrization (KPP; Large et al., 1994). The 48-member ensemble outputs used in this study are instantaneous snapshots every five days starting at 00:10, January 1, 1967; no temporal averaging has been applied. By this date, four years after the initial ensemble generation, ensemble statistics have saturated. Similar spectral analyses at location A, performed on the same date at 10-year intervals in the available 50 years of five-day averaged outputs (not shown) produce statistically equivalent results.

Prior to taking the wavelet transforms, the fields were linearly interpolated onto a uniform grid. In order to account for the finite-volume discretization of MITgcm, we first weighted the velocity fields by the grid area. The velocities were then linearly interpolated onto the uniform grid and divided by the area also interpolated onto the uniform grid. The uniform grid spacings were taken as the minimum spacing per $10^\circ \times 10^\circ$ domain centered around each location in Fig. 1. The wavelet transforms are taken at the single grid point at the center of the $10^\circ \times 10^\circ$ domain while the fast Fourier transforms (FFTs) are taken over the $10^\circ \times 10^\circ$ domain.

3.1. The wavelet and Fourier approach

One of the major differences between quasi geostrophy and primitive equations is that advection is two-dimensional (2D) in the former and three-dimensional (3D) for the latter. It can be argued that for primitive equations, the eddy velocity defined about the thickness-weighted averaged residual mean, which reduces to 2D under adiabatic conditions, corresponds to the QG eddy velocities under order-Rossby number fluctuations in the layer thickness (Young, 2012; Marshall et al., 2012; Maddison and Marshall, 2013; Aoki, 2014; Loose et al., 2022; Uchida et al., 2023a; Meunier et al., 2023). Nonetheless, the spectral flux of KE and enstrophy have commonly been examined in geopotential coordinates (e.g. Capet et al., 2008; Arbic et al., 2013; Khatri et al., 2018, 2021; Ajayi et al., 2021; Storer et al., 2022). Due to the discrepancies between quasi geostrophy and primitive equations in geopotential coordinates, there is no guarantee that the inertial-range theory should hold for the latter. In this section, we examine the agreement between the wavelet and Fourier approach, and to what extent the spectra and spectral fluxes in geopotential coordinates are consistent with QG predictions. We also include contributions from vertical advection unlike studies using satellite observations where only the horizontal velocities are available (Scott and Wang, 2005).

3.1.1. Spectral Estimates

We start by comparing the wavenumber spectra of eddy-KE (EKE; Table 1) derived from wavelet and traditional Fourier methods at locations A and B. While wavenumber spectra have commonly been computed for total-KE, our interest in EKE stems from geostrophic turbulence alluding to eddies. Prior to taking the Fourier transform, land cells surrounded by ocean were linearly interpolated over and filled in with zeros otherwise. A standard Hann window was then applied to make the data doubly periodic. No windowing was applied to the wavelet approach. In all cases, bootstrapped confidence intervals are provided by randomly resampling (with replacement) from the 48 ensemble member energy densities 9999 times.

As shown in Fig. 3, the two approaches agree well in their spectral estimates. Such a similarity between Fourier and wavelet estimates have also been identified in doubly periodic homogeneous QG simulations where Fourier modes are best suited (Uchida et al., 2023b). As expected, EKE at location A is orders of magnitude larger than at location B. The wavelet spectra peak around 300 - 500 km for both locations, a feature the Fourier approach is unable to capture due to low wavenumber resolution at small wavenumbers. The overall spectral slopes are around -3 at the surface but steepen with wavenumber and significantly below the mixed layer. A least-squares best fit to the spectra between roughly 250 - 80 km at $z = -452$ m suggests a -3.93 and -3.75 power law at locations A and B respectively, which is considerably steeper than either the $-5/3$ or -3 energy and enstrophy inertial-range laws emerging from standard scaling analysis of quasi geostrophy.

3.1.2. Spectral Budgets

In the ocean, it is unlikely that the sources and sinks of energy are localized in wavenumber as assumed by standard, idealized inertial-range theories. Estimates of the scale-dependence can be made by explicitly computing wavelet-transforms of the 'dynamics', i.e. transforms of all the terms in the spectral budget of eddy momentum

$$\mathcal{T}_K = \mathcal{P}_K + \mathcal{A}_K + \mathrm{MtE}_K + \mathcal{D}_K \,, \tag{11}$$

where the notations are summarized in Table 1. A derivation of each term is given in Appendix A. Our form of pressure work consists only of the wavelet transforms related to $-\langle \boldsymbol{u}' \cdot \nabla_{\mathrm{h}} \phi' \rangle$. Adding and subtracting $\langle w'b' \rangle$ respectively and using the hydrostatic relationship demonstrates that exchanges between potential and kinetic energies are contained in this term (e.g. Uchida et al., 2024). We do not consider potential energy explicitly here, leaving this as a topic for consideration elsewhere.

The relative contributions of terms in the spectral budget computed at location A are shown in Fig. 4 where the residual (grey dashed line) is seen to be negligible. Namely, we are able to close the EKE spectral budget with wavelets, exemplifying their utility. Positive values indicate a source for the EKE reservoir and negative values a sink at a given wavenumber. At the surface, the balance is largely between pressure work and dissipation due to KPP (Fig. 4a), an indication of turbulent Ekman dynamics carrying significance and pressure work counterbalancing Ekman transport. Although peaking at scales about 300 km, dissipation is broadband in wavenumber. Below the mixed layer, contribution from convective events reduce significantly ($\mathcal{D}_K \sim 0$) and the largest values from the dynamics belong to pressure work and advection, which sum up to the tendency (Fig. 4b). However, all the quantities, except for advection with positive values, are indistinguishable from zero at the 95% confidence level.

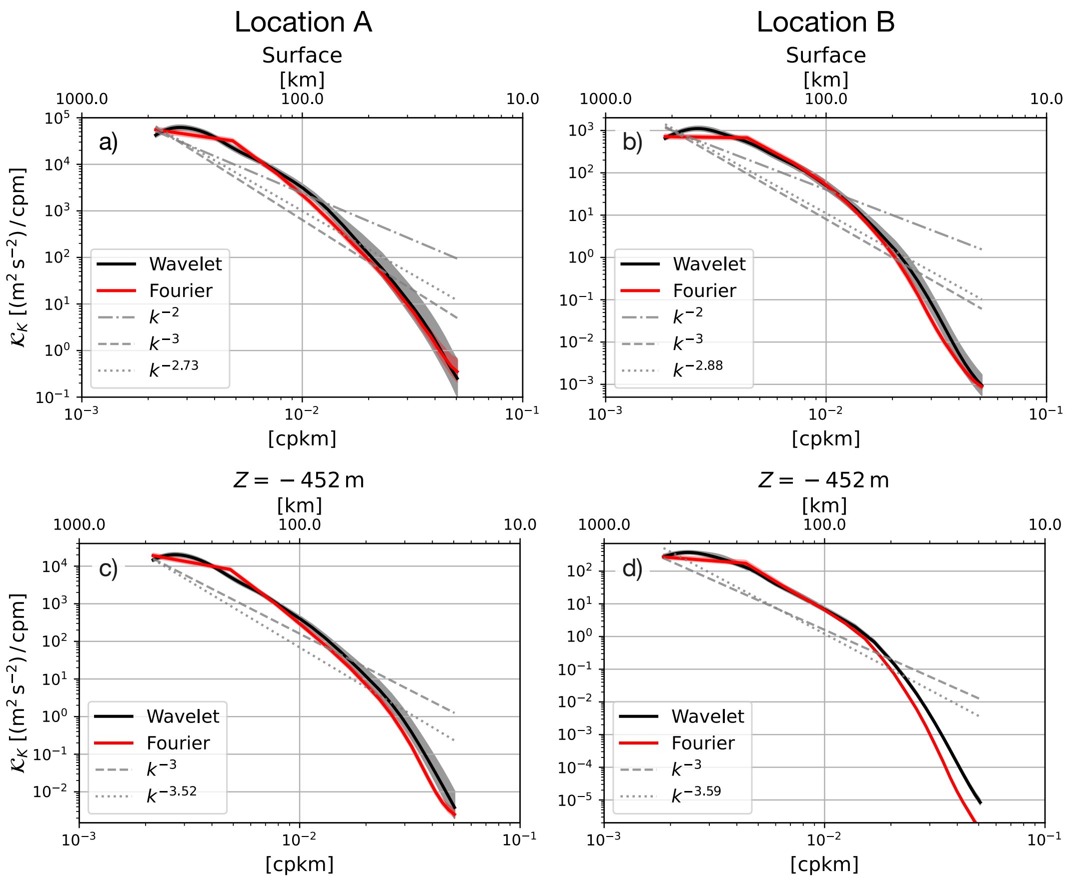

Figure 3: Isotropic (azimuthally-integrated) EKE spectrum $\mathscr{K}_K(k)$ using the wavelet and FFT approach from $z = -3\,\mathrm{m}$ (top) and $z = -452\,\mathrm{m}$ (bottom) at locations A (left) and B (right; indicated in Fig. 1). The wavelet spectra is shown as black curves and Fourier as red curves on January 1, 1967. The land cells are interpolated over for the FFT approach. The colored shadings indicate the 95% bootstrap confidence interval. Power law with the slope of -2 is indicated with grey dotted-dashed lines, -3 with grey dashed lines and a best fit between 250 - 80 km with grey dotted lines.

As an effort to reduce the uncertainty in the spectral budget, we exhibit the budget when it is spatial averaged over eight neighboring grid points of location A (viz. nine grid points in total including location A; Fig. 4c). The spatial averaging is taken after the wavelet budget is computed at each grid point for each ensemble member. Indeed, we are leveraging the spatial locality of wavelet transform (4) at each grid point. In this context, Fourier spectra can be considered as a spatial average of spectral estimates over the entire $10° \times 10°$ domain centered about location A (equivalent to 120×116 grid points; Uchida et al., 2021c). Comparing Figs. 4b and 4c, the uncertainty noticeably reduces by merely averaging the spectral estimates over neighboring nine grid points while capturing the local properties in space within the Gulf Stream extension. Namely, the mean estimate in solid curves remain nearly identical between Figs. 4b and 4c. We acknowledge that neighboring points are likely correlated with each other so the degrees of freedom in estimating the uncertainty is smaller than 9×48 upon averaging over nine grid points. Upon examining the uncertainty when averaged over four grid points, the uncertainty decreased compared to Fig. 4b but was still larger than Fig. 4c (not shown). The non-conservative term is expected to be very small as we are below the mixed layer ($\mathcal{D}_K \sim 0$). The advection $\mathcal{A}_K$ is positive across all wavenumbers, which would imply a forward cascade of energy (blue curve in Fig. 4c). The pressure work term, while noisy, tends to peak at around 250 km (red curve in Fig. 4c), so QG theory might argue for an upscale energy cascade at smaller wavenumbers (Vallis, 2006). This is not what we find (i.e. $\mathcal{A}_K > 0$), however, arguing for a deviation from quasi geostrophy in our results. The forward KE cascade in the vicinity of Gulf Stream separation has also been documented in previous studies (Aluie et al., 2018; Contreras et al., 2023). While small in magnitude, the energy input from shear production tends to be positive at the smallest wavenumbers ($\mathrm{MtE}_K \gtrsim 0$; green curve in Fig. 4c). In conjunction with a forward EKE cascade, it is likely that around location A, the eddies are forced by the mean flow at largest scales, which drives a downscale cascade.

While the Fourier approach is also able to close the budget (Fig. 4d), in contrast to the spectra (red curves in Fig. 3), the uncertainty in Fourier estimates of the spectral budget is much larger than the wavelets estimates (Fig. 4c). This is surprising because Fourier transform is based on a two-point correlation function which is a global operator and results in a spatially averaged estimate over the entire domain of which the transform is taken (Uchida et al., 2021c). The large uncertainty is partially due to windowing artifacts at smaller wavenumbers given that the uncertainty increases with decreasing wavenumber (cf. Aluie et al., 2018; Uchida et al., 2023b), and potentially attributable to conflating different dynamical regimes within an inhomogeneous flow, e.g. the relatively narrow separated Gulf Stream path and flows about it.

Figure 5 documents the spectral budget at location B. Similar to location A, at the surface, the balance is largely between pressure work and dissipation. At the smallest wavenumbers, the energy input from wind stress is negative ($\mathcal{F}_K < 0$, cyan curve in Fig. 5a; Renault et al., 2016; Uchida et al., 2024). The uncertainty is large but again notably reduces when averaged over neighboring nine grid points around location B while retaining the same structure in the mean spectral estimates (solid curves in Fig. 5b, c). Interestingly, unlike about location A where there is a persistent mean flow, the shear production is negligible ($\mathrm{MtE}_K \sim 0$). The Fourier estimate is severely hampered by the windowing effect and low wavenumber resolution at small wavenumbers (Fig. 5d).

Hereon, the wavelet spectra are computed at a single grid point while the spectral budgets and fluxes are averaged over nine neighboring grid points given the size of uncertainty (Figs. 3, 4c and 5c). We will also focus on below the mixed layer ($z = -452$ m) where energy input from surface convection is negligible.

3.1.3. Spectral Fluxes

Using the wavelet transforms, we can also diagnose the spectral flux of EKE

$$
\begin{aligned}
\varepsilon_K(\boldsymbol{\gamma},\phi,k) &= -\frac{1}{C_\Xi}\int_{k>\kappa}\mathcal{R}\left[\left\langle\tilde{u'}^*\widetilde{(\boldsymbol{v}\cdot\nabla u')}\right\rangle+\left\langle\tilde{v'}^*\widetilde{(\boldsymbol{v}\cdot\nabla v')}\right\rangle\right]x_0^2\kappa\,\mathrm{d}\kappa \\
&= -\frac{1}{C_\Xi}\int_{k>\kappa}\mathcal{R}\left[\left\langle\tilde{u'}^*\widetilde{(\boldsymbol{v}\cdot\nabla u)'}\right\rangle+\left\langle\tilde{v'}^*\widetilde{(\boldsymbol{v}\cdot\nabla v)'}\right\rangle-\left\langle\tilde{u'}^*\widetilde{\boldsymbol{v'}\cdot\nabla\langle u\rangle}\right\rangle-\left\langle\tilde{v'}^*\widetilde{\boldsymbol{v'}\cdot\nabla\langle v\rangle}\right\rangle\right]x_0^2\kappa\,\mathrm{d}\kappa \\
&= \int_{k>\kappa}\mathcal{A}_K(\boldsymbol{\gamma},\phi,\kappa)\,\mathrm{d}\kappa\,, \qquad (12)
\end{aligned}
$$

where $\boldsymbol{v}=\boldsymbol{u}+w\boldsymbol{e}_3$ is the three-dimensional velocity, $\boldsymbol{e}_3$ the vertical unit vector, $\mathcal{R}[\cdot]$ indicates the real part and κ is a dummy variable (Table 1). Positive values indicate a forward cascade towards smaller scales and negative values an inverse cascade towards larger scales. The EKE spectral flux (12) is re-arranged in a way to achieve machine precision in the spectral budget (Appendix A) but corresponds to

$$
\left\langle\boldsymbol{v}\cdot\nabla\frac{|\boldsymbol{u}'|^2}{2}\right\rangle=\left\langle u'\left[(\boldsymbol{v}\cdot\nabla u)'-\boldsymbol{v}'\cdot\nabla\langle u\rangle\right]\right\rangle+\left\langle v'\left[(\boldsymbol{v}\cdot\nabla v)'-\boldsymbol{v}'\cdot\nabla\langle v\rangle\right]\right\rangle\,. \qquad (13)
$$

Figure 6 shows the isotropic (azimuthally-integrated) spectral flux of EKE for both the Fourier and wavelet approaches. There is a general agreement between the two estimates (within 95% confidence intervals) and both approaches indicate a forward EKE cascade at all available spatial scales (Fig. 6), although its significance is much smaller about location B. Neither location indicates the existence of an inertial range where the energy flux might be considered scale independent and constant over a range of wavenumbers. The forward cascade about location A is likely powered by the energy exchange with the mean flow at the smallest wavenumbers (Fig. 4c). Consistent with the budgets, the Fourier spectral flux has much larger uncertainties than the wavelet approach, the former likely affected by the windowing procedure (cf. Aluie et al., 2018; Uchida et al., 2023b). Physically, the divergence in the ensemble-mean estimates between the two approaches is attributable to the EKE flux locally about locations A and B compared to the flux averaged over the $10^\circ\times10^\circ$ domains.

3.2. Oriented spectra and spectral flux

At any spatial location, $\boldsymbol{\gamma}$, we compute $\mathscr{K}_K(k,\phi)$ for 18 orientation angles taken between $\phi=[0,\pi)$. We define energy maximal/minimal angles as those angles resulting in the maximum/minimum integrated energy across all scales in the wavelet decomposition. Plots of the wavelet spectra at energy maximal/minimal wavelet orientation angles, along with the respective angles, are shown for locations A and B in Fig. 7. The directions of maximum and minimum energy are nearly orthogonal and closely coincide, respectively, with the meridional and zonal directions at both locations.

We first examine the location close to the Gulf Stream separation point, as seen in Fig. 1 (location A; Fig. 7a), which exhibits the highest energy levels (close to $10^3\,(\mathrm{m^2\,s^{-2}})/\mathrm{cpm}$) within the North Atlantic basin. Figures 3b and 7a differ in the fact that the former is azimuthally integrated while the latter is not. A dashed line indicating a -3 slope appears in grey; the spectrum aligned with the angle associated with maximum energy has a shallower slope than the angle associated with minimum energy but still tends to be steeper than -3 at lower wavenumbers, and then transitions to an even steeper decay for higher wavenumbers as already observed in Fig. 3b. A statistically significant signal of anisotropy is apparent, characterized by enhanced energy in the meridional direction relative to the zonal direction. This is likely an imprint of the Gulf Stream on the eddy field due to the roughly zonal orientation of the separated Gulf Stream.

Location B (Fig. 7b) comes from ostensibly the interior of the general circulation where one might anticipate QG dynamics would govern. Mean flows are weak and do not exhibit much structure on the deformation scale, generating conditions in which isotropy might be anticipated. In accord with these expectations, the energy level is much lower than location A. Beyond this, however, the results are quite surprising. Most unexpectedly, the spectra exhibit statistically significant anisotropy, in a sense similar to that at location A. Namely, North-South (nominally) spectra are more energetic than East-West spectra. The spectral slope in the North-South direction is close to -3 but is steeper in the East-West direction. This is difficult to ascribe to canonical isotropic QG dynamics. In short, our quantitative measures of the eddy field in the ocean interior do not meet with inertial-range expectations.

Aligned with the orientation of maximum and minimum levels of EKE, the EKE spectral flux are shown (Fig. 7c, d). There is a rough correspondence between the spectra and flux where the angle with the least amount of EKE with steepest spectral slope is associated with a larger forward cascade of EKE. Conversely, the angle with the highest amount of EKE and shallowest spectral slope indicates an inverse cascade.

Along with the spectra, we exhibit the eddy anisotropy angles defined as (Waterman and Lilly, 2015)

$$\vartheta = \frac{1}{2}\arctan\left(\frac{2\langle u'v'\rangle}{\langle u'^2 - v'^2\rangle}\right) . \tag{14}$$

The angles north of 30°N show no coherent patterns while there is some indication of a slight north-eastward self-organization of angular patterns south of 30°N (Fig. 8), which may be resulting from beta-plane turbulence (Maximenko et al., 2005; Galperin et al., 2004, 2006). In particular, Danilov and Gurarie (2004) demonstrated that under beta-plane turbulence, isotropic energy spectra had higher power than zonal energy spectra across all spatial scales, which tends to be consistent with the anisotropy we observe in our spectra.

3.3. Temporal variability

The ensemble dimension allows us to examine the temporal variability of the wavenumber spectra. The temporal stability of the results above can be assessed by conducting the same analysis on data five and 10 days later in time. The energy input from the mean flow to eddies remains positive and relatively stationary over time at location A ($\mathrm{MtE}_K > 0$; green curves in Figs. 4c and 9c, e). It is negligible at location B ($\mathrm{MtE}_K \sim 0$; Figs. 5c and 9d, f).

$\mathcal{T}_K$ largely fluctuates with $\mathcal{P}_K$ at both locations A and B (Fig. 9c - f) and is not stable in sign. Namely, the pressure work is largely passed onto the tendency term, which might suggest signals propagating through location A from its surroundings. As the ensemble mean, which captures the oceanic response to atmospheric forcing, is removed from the spectral calculations, the signals are likely due to oceanic intrinsic variability including mesoscale eddies and perhaps also planetary waves. In contrast, the spectral flux is persistently positive and significant at the 95% level for scales above $\sim$ 50 km at both locations (Fig. 9g, h). Despite the large fluctuations in EKE tendency, the spectra seem remarkably stable in time (they are virtually indistinguishable from each other through January $1-11$; Figs. 9a, b).

Figure 10 documents the EKE and slopes of isotropic EKE spectra at the surface and $z = -452$ m throughout the year of 1967. The slopes at the surface tend to be shallower than at depth. Consistent with previous studies (e.g. Uchida et al., 2017; Ajayi et al., 2020; Khatri et al., 2021), there seems to be a seasonality of shallower slopes during winter-to-spring and steeper slopes during summer-to-autumn at the surface but the seasonal signal tends to be dulled at depth. Interestingly, the shallower slopes do not directly translate to higher levels of EKE at the surface (dashed curves in Fig. 10a, b). Focusing on below the mixed layer, the EKE spectral flux largely tends to be positive about location A (Fig. 10c) but an inverse EKE cascade emerges about location B between spring and autumn (March - November) at scales of 250 km (Fig. 10e). At location A, shear production from the mean flow is overall positive ($\mathrm{MtE}_K \gtrsim 0$; Fig. 10d). While MtE_K is predominantly negative at location B, the magnitude of it is an order smaller than the spectral flux (Fig. 10f).

We end this section by documenting the annual mean of the ensemble-averaged wavelet-based isotropic spectral budget and flux at location A and B. The temporal averaging was applied by taking the ensemble-based budgets every 15 days to allow for temporal decorrelation. At location A, the large fluctuations in pressure work and EKE tendency tend to die off at scales below 300 km (Fig. 11a). Shear production from the mean flow seems relatively stable in time, which implies a stable mean Gulf Stream, and is always in the direction of energizing the eddies at the largest scales ($\mathrm{MtE}_K > 0$; Figs. 4c, 9a, c and 11a). Interestingly, at location B the signal of pressure work persists and remains a leading-order term in the EKE budget (Fig. 11b). Shear production at this location from the mean flow remains negligible. The EKE spectral flux indicate a forward cascade at location A across all scales (Fig. 11c) while an inverse cascade emerges at scales larger than 200 km for location B (Fig. 11d). In conjunction with Figs. 9f and 10e, this implies that even though the EKE cascade is upscale as a net over time at location B, consistent with previous studies examining the time-mean view of EKE cascade, there are times where the cascade can be downscale.

4. Conclusions and discussion

Using a relatively novel wavelet approach applied to an ensemble of eddy-rich North Atlantic simulations, we claim we can compare local oceanic eddy-kinetic energy (EKE) spectra from several spots within the general circulation characterized by vastly different dynamics (Grooms et al., 2011). While some studies have expanded their analyses to characterize the spectral structure on a global scale (Storer et al., 2022, 2023), here, we have been interested in the other tail end of the spatial range. Specifically, we compare spectra locally within the Gulf Stream extension to those found in the gyre interior. The motivation for these comparisons arise from: i) a parameter-free definition of an 'eddy', and ii) interest in clarifying the description of eddies in this heterogeneous field dominated by an ensemble-mean Gulf Stream and relatively quiescent interior. We anticipated that the Gulf Stream would imprint the eddy field with an anisotropic structure, but that the gyre interior would be much simpler and isotropic (Pedlosky et al., 1987). Although earlier studies had warned that the separated Gulf Stream might not be quasi-geostrophic (QG; Aluie et al., 2018; Jamet et al., 2020b; Contreras et al., 2023), we nonetheless expected to see evidences of up-scale energy cascades at scales beyond the deformation radius, and down-scale cascades at shorter length scales.

Several relatively robust characteristics emerge from our calculations, almost none of which aligned with our hypotheses. As expected, the near separation Gulf Stream was found to be anisotropic at the 95% confidence level. However, beyond this, our analysis yielded surprising results. An examination of spectral flux in the near Gulf Stream argued for down scale energy cascades across the spectrum and yielded essentially no evidence for an up-scale flux (Figs. 6 and 10), although the inverse cascade emerges later into the year about location B. The forward EKE cascade in the Gulf Stream extension is likely powered by the energy input from the mean flow at the largest scales (Figs. 4c, 9a, c and 10c). Conversely, the input from mean flow to the eddies being negligible at location B likely allows for the inverse EKE cascade to emerge. We also find that the direction of energy cascade is time and angle dependent, a deviation from inertial-range arguments where stationarity and isotropy are assumed.

In summary, we argue the North Atlantic eddy field is found in an unavoidably inhomogeneous environment (Uchida et al., 2021c), and exhibits characteristics that we currently have little theoretical guidance to interpret. The steep spectral slopes could be ascribed to numerical viscosity (Arbic et al., 2013; Uchida et al., 2017), intermittency in the turbulence cascade (Vallis, 2006), surface quasi geostrophy (SQG) with a varying interior stratification (Callies and Ferrari, 2013; Yassin and Griffies, 2022), or deviation from quasi geostrophy in the Gulf Stream region. A regime governed by SQG would result in a shoaling of the spectral slope towards the surface, which is what we indeed see from Figs. 3 and 10b. It is unclear, however, how deep into the real ocean SQG would penetrate as the governing mechanism for turbulence (Miracca-Lage et al., 2022; Liu et al., 2023). The steepness is also partially attributable to the lack of submesoscale turbulence in our ensemble, which has been demonstrated to shoal the EKE spectra (Capet et al., 2008; Chassignet and Xu, 2017; Ajayi et al., 2020; Schubert et al., 2020; Khatri et al., 2021), and us analyzing below the surface mixed layer where mixed-layer instability occurs (Boccaletti et al., 2007; Özgökmen et al., 2011; Uchida et al., 2017, 2019, 2022c). Preliminary findings show, however, that even at $1/50°$ resolution, the spectral slope remains significantly steeper than -3 below the mixed layer ($z = -412\,\mathrm{m}$) in the separated Gulf Stream region (Supplementary Material; Figs. S2 and S3). In the highly stratified Gulf Stream region, the presence of leading-order vortex-tube stretching may be emphasized, a deviation from quasi geostrophy where isopycnal fluctuations are constrained to be on the order of small Rossby number. Further examination on the level of deviation from (surface) quasi geostrophy below the mixed layer is left for future work but there is some indication from in-situ observations that our steep spectral slopes in the interior may not merely be a model artifact (Steinberg and Eriksen, 2022, their Fig. 10, panel sg045). While our ensemble was never developed with the observations of the Deep Western Boundary Current in mind, it is able to capture the KE variability about frequencies corresponding to 30 - 50 days observed in the Line W mooring data (Supplementary Material, Fig. S1; Andres et al., 2016). Finally, and perhaps most unexpectedly, anisotropy in the computed spectra is apparent at a location within the gyre interior, a location where we *a priori* expected it to be horizontally isotropic; the anisotropy could be an artifact of beta-plane turbulence (Fig. 7).

The goals of this paper were to apply the wavelet-based technique for estimating the EKE wavenumber spectra and its spectral flux in realistic simulations where the usual assumptions of homogeneity and isotropy are clearly suspect. We have demonstrated that the wavelet method is not inconsistent with the canonical Fourier approach but with the additional strengths of: i) negating the necessity for the data to be periodic, ii) flexibility in defining the wavenumber resolution via the scaling s, and iii) being able to extract the local anisotropy in the flow through the rotational matrix R (cf. Uchida et al., 2023b). As was noted in Uchida et al. (2023b), our approach is complementary to the growing body of literature on spectral methods attempting to overcome the shortcomings of the Fourier approach: Aluie et al. (2018); Sadek and Aluie (2018); Schubert et al. (2020); Zhao et al. (2022); Buzzicotti et al. (2023) and Tedesco et al. (2023) where they use a spatial filter to examine the KE spectra and cross-scale transfer, Lindborg (2015); Balwada et al. (2016, 2022); LaCasce (2016); Poje et al. (2017) and Pearson et al. (2020) where they implement structure functions, Jamet et al. (2020a) where they employ a Green's function, and Uchida et al. (2021c) where they use Empirical Orthogonal Functions. Barkan et al. (2021) and Srinivasan et al. (2022) apply the filtering method in both the spatiotemporal dimensions. It is true that the eddy field is not expected to be stationary, although this is a topic that has not received serious attention in this paper. Based on characteristic time scale arguments $\tau = \mathscr{K}_K/\mathcal{T}_K$, one might expect the spectra at scales above 100 km to vary on the timescales of $\tau \sim 10^4 - 10^5$ seconds $\simeq 0.1-1$ days looking at Figs. 3c, d, 4c, 5c and 9. Interestingly, EKE and its spectra below the mixed layer seem remarkably stable over time (Figs. 3, 9a, b and 10a, b) whereas its tendency $\mathcal{T}_K$ fluctuates rapidly with time (Figs. 4, 5 and 9c - f). While the ensemble technique permits the examination of the time dependence of eddy spectra and spectral flux, we have only touched upon it here (Fig. 10). A more complete examination of the cross-scale eddy energy transfers is also desirable and possible within the ensemble framework. And with it, one can examine in more detail the eddy dynamics to address the question of anisotropic up- and down-scale energy transfers. These are amongst the next set of items we intend to address.

A highly related and separate issue involves the examination of potential energy fluxes. We have here looked solely at the KE spectra. QG theory in its predictions for up and down scale cascades involves the combined kinetic and potential energies of the flow (Vallis, 2006).

However, in contrast to QG theory, where the resulting total energy is quadratic and positive definite, primitive equation settings in geopotential coordinates bring no such guarantees as dynamic enthalpy is virtually a linear term ($h = \int g^{-1} b(\Theta, S, \Phi)\,\mathrm{d}\Phi$; Young, 2010; Uchida et al., 2024) and buoyancy b is not sign definite where Θ is conservative temperature, S is absolute salinity and Φ is the dynamically non-active part of hydrostatic pressure; the TWA framework, on the other hand, suggests a (quadratic) positive-definite total eddy energy when the equation of state for density is linear or when the amplitude of perturbations are on the order of small Rossby number (cf. Maddison and Marshall, 2013; Aoki, 2014; Loose et al., 2022; Uchida et al., 2022b, their Appendix A). How to address the role of potential energy in non-linear cascades and its impact on KE anisotropy is left for future work.

Data availability statement

The open-source parallelized FFT and wavelet-transform Python packages are available via Github (Uchida et al., 2021d; Uchida and Dewar, 2022). Jupyter notebooks used to conduct the analysis are available via Github (`https://github.com/roxyboy/NA-wavelet-notes/tree/master/Snapshots`; a DOI will be added upon acceptance of the manuscript). The simulation outputs are available on the Florida State University cluster (`http://ocean.fsu.edu/~qjamet/share/data/Uchida2021/`). The Line W mooring data was downloaded from `https://hdl.handle.net/1912/28669`.

Declaration of competing interest

The authors declare no conflict of interest.

Acknowledgements

We thank the editor Yisen Zhong along with two anonymous reviewers for their careful reading of our manuscript. This study is a contribution to the 'Assessing the Role of forced and internal Variability for the Ocean and climate Response in a changing climate' (ARVOR) project supported by the French 'Les Enveloppes Fluides et l'Environnement' (LEFE) program. W. K. Dewar is supported through NSF grants OCE-1829856, OCE-1941963 and OCE-2023585, and the French 'Make Our Planet Great Again' (MOPGA) program managed by the Agence Nationale de la Recherche under the Programme d'Investissement d'Avenir, reference ANR-18-MPGA-0002. The latter two grants served as the primary support for T. Uchida and partially for Q. Jamet. A. Poje acknowledges support from the NSF grant OCE-2123633. High-performance computing resources on Cheyenne and Derecho (`doi:10.5065/D6RX99HX`) used for running the NA ensembles were provided by NCAR's Computational and Information Systems Laboratory, sponsored by NSF, under the university large allocation UFSU0011 and UFSU0023. We would like to thank Edward Peirce and Kelly Hirai for maintaining the FSU Comedians cluster on which the data were analyzed. The MITgcm outputs were read using the `xmitgcm` Python package (Abernathey et al., 2022) and postprocessed with the `xgcm` Python package (Abernathey et al., 2021).

Appendix A. Spectral budget

One of the desirable properties of taking the averaging over the ensemble dimension is that the wavelet transform and averaging operator commute with each other, i.e. $\langle\tilde{\cdot}\rangle = \widetilde{\langle\cdot\rangle}$, owing to the ensemble dimension being orthogonal to the spatiotemporal dimensions.

Appendix A.1. Total kinetic energy

The MITgcm `diagnostics` outputs were saved for each term in the total momentum budget

$$\boldsymbol{u}_t + \boldsymbol{v}\cdot\nabla\boldsymbol{u} + \boldsymbol{f}\times\boldsymbol{u} = -\nabla_{\mathrm{h}}\phi + \boldsymbol{\mathcal{X}}\,, \tag{A.1}$$

where $\boldsymbol{\mathcal{X}}$ is the non-conservative diabatic term consisting of dissipation and contribution from KPP. The spectral budget of total kinetic energy (TKE; $K = |\boldsymbol{u}|^2/2$) is constructed by taking the dot product of total horizontal momentum vector with (A.1)

$$K_t + \boldsymbol{v}\cdot\nabla K = -\boldsymbol{u}\cdot\nabla_{\mathrm{h}}\phi + \boldsymbol{u}\cdot\boldsymbol{\mathcal{X}}\,. \tag{A.2}$$

Thus, the mean TKE spectral budget becomes

$$\frac{1}{C_\Xi}\langle\tilde{\boldsymbol{u}}^*\cdot\tilde{\boldsymbol{u}}_t\rangle\, x_0^2k = -\frac{1}{C_\Xi}\left\langle\tilde{\boldsymbol{u}}^*\cdot\widetilde{\nabla_{\mathrm{h}}\phi}\right\rangle x_0^2k - \frac{1}{C_\Xi}\left[\left\langle\tilde{u}^*\widetilde{(\boldsymbol{v}\cdot\nabla u)}\right\rangle + \left\langle\tilde{v}^*\widetilde{(\boldsymbol{v}\cdot\nabla v)}\right\rangle\right] x_0^2k + \frac{1}{C_\Xi}\left\langle\tilde{\boldsymbol{u}}^*\cdot\tilde{\boldsymbol{\mathcal{X}}}\right\rangle x_0^2k\,. \tag{A.3}$$

C_Ξ is computed using the `xrft` Python package (Uchida et al., 2021d). The horizontal KE spectral flux often examined by other studies is encapsulated in the advective terms of (A.3).

Appendix A.2. Mean kinetic energy

The ensemble mean kinetic energy (MKE; $K^\# = |\langle\boldsymbol{u}\rangle|^2/2$) equation is given by taking the dot product of mean momentum vector with each terms in the mean momentum equation

$$\langle\boldsymbol{u}_t\rangle + \langle\boldsymbol{v}\rangle\cdot\nabla\langle\boldsymbol{u}\rangle + \langle\boldsymbol{v}'\cdot\nabla\boldsymbol{u}'\rangle + \boldsymbol{f}\times\langle\boldsymbol{u}\rangle = -\langle\nabla_{\mathrm{h}}\phi\rangle + \langle\boldsymbol{\mathcal{X}}\rangle\,, \tag{A.4}$$

viz.

$$\begin{aligned} K_t^\# + \langle\boldsymbol{v}\rangle\cdot\nabla K^\# &= -\langle\boldsymbol{u}\rangle\cdot\nabla_{\mathrm{h}}\langle\phi\rangle - \langle u\rangle\nabla\cdot\langle\boldsymbol{v}'u'\rangle - \langle v\rangle\nabla\cdot\langle\boldsymbol{v}'v'\rangle + \langle\boldsymbol{u}\rangle\cdot\langle\boldsymbol{\mathcal{X}}\rangle \\ &= -\langle\boldsymbol{u}\rangle\cdot\nabla_{\mathrm{h}}\langle\phi\rangle - \left[\nabla\cdot\left\langle\boldsymbol{v}'\cdot(\langle\boldsymbol{u}\rangle\cdot\boldsymbol{u}')\right\rangle - \langle\boldsymbol{u}'\boldsymbol{v}'\rangle\cdot\nabla\langle\boldsymbol{u}\rangle\right] + \langle\boldsymbol{u}\rangle\cdot\langle\boldsymbol{\mathcal{X}}\rangle\,. \end{aligned} \tag{A.5}$$

On the other hand, in obtaining the MKE budget terms to machine precision, we re-run MITgcm every five days from the ensemble-mean state. Equivalently, we solve for the momentum equation as a initial-value problem where the initial condition is given as the ensemble mean state every five days

$$\langle\boldsymbol{u}_t\rangle + \langle\boldsymbol{v}\rangle\cdot\nabla\langle\boldsymbol{u}\rangle + \boldsymbol{f}\times\langle\boldsymbol{u}\rangle = -\langle\nabla_{\mathrm{h}}\phi\rangle + \langle\boldsymbol{\mathcal{X}}\rangle\,, \tag{A.6}$$

and MITgcm `diagnostics` outputs were saved for each term in (A.6) upon running it for a few time steps. This allows us to diagnose the divergence of the Reynolds stress, $\nabla\cdot\langle\boldsymbol{v}'\boldsymbol{u}'\rangle$, to machine precision by taking the difference between the ensemble mean of total momentum equation (A.4) and (A.6). Taking the dot product of the mean momentum vector with (A.6) yields the *prognostic* MKE (pMKE) budget as an initial-value problem

$$K^{\#}_t + \langle\boldsymbol{v}\rangle\cdot\nabla K^{\#} = -\langle\boldsymbol{u}\rangle\cdot\nabla_{\mathrm{h}}\langle\phi\rangle + \langle\boldsymbol{u}\rangle\cdot\langle\boldsymbol{\mathcal{X}}\rangle\,. \tag{A.7}$$

Notice that (A.7) differs from (A.5) by $\nabla\cdot\big\langle\boldsymbol{v}'\cdot(\langle\boldsymbol{u}\rangle\cdot\boldsymbol{u}')\big\rangle - \langle\boldsymbol{u}'\boldsymbol{v}'\rangle\cdot\nabla\langle\boldsymbol{u}\rangle$.

Appendix A.3. Eddy kinetic energy

TKE can be expanded as

$$\begin{aligned} K &= \frac{1}{2}|\langle\boldsymbol{u}\rangle + \boldsymbol{u}'|^2 \\ &= K^{\#} + \mathscr{K} + \langle\boldsymbol{u}\rangle\cdot\boldsymbol{u}'\,, \end{aligned} \tag{A.8}$$

where $\mathscr{K} = |\boldsymbol{u}'|^2/2$ so

$$\begin{aligned} \langle\boldsymbol{v}\cdot\nabla K\rangle &= \big\langle(\langle\boldsymbol{v}\rangle + \boldsymbol{v}')\cdot\nabla(K^{\#} + \mathscr{K} + \langle\boldsymbol{u}\rangle\cdot\boldsymbol{u}')\big\rangle \\ &= \langle\boldsymbol{v}\rangle\cdot\nabla K^{\#} + \Big\langle\big(\langle\boldsymbol{v}\rangle + \boldsymbol{v}'\big)\cdot\nabla\mathscr{K}\Big\rangle + \langle\boldsymbol{v}'\cdot\nabla(\langle\boldsymbol{u}\rangle\cdot\boldsymbol{u}')\rangle\,. \end{aligned} \tag{A.9}$$

Hence, subtracting (A.5) from the ensemble mean of (A.2) yields

$$\langle\mathscr{K}\rangle_t + \langle\boldsymbol{v}\cdot\nabla\mathscr{K}\rangle = -\langle\boldsymbol{u}'\cdot\nabla_{\mathrm{h}}\phi'\rangle - \langle\boldsymbol{u}'\boldsymbol{v}'\rangle\cdot\nabla\langle\boldsymbol{u}\rangle + \langle\boldsymbol{u}'\cdot\boldsymbol{\mathcal{X}}'\rangle\,, \tag{A.10}$$

where we see the mean flow and eddies exchanging energy via the term $\langle\boldsymbol{u}'\boldsymbol{v}'\rangle\cdot\nabla\langle\boldsymbol{u}\rangle$ sometimes referred to as shear production in the turbulence literature.

In order to achieve machine precision in closing the eddy kinetic energy (EKE) budget using the MITgcm `diagnostics` package outputs, we rearrange (A.10) as

$$\begin{aligned} \langle\mathscr{K}\rangle_t &= -\langle\boldsymbol{u}'\cdot\nabla_{\mathrm{h}}\phi'\rangle - \underbrace{\big(\langle\boldsymbol{v}\cdot\nabla\mathscr{K}\rangle + \langle\boldsymbol{u}'\boldsymbol{v}'\rangle\cdot\nabla\langle\boldsymbol{u}\rangle\big)}_{=\langle\boldsymbol{u}'\cdot(\boldsymbol{v}\cdot\nabla\boldsymbol{u})'\rangle} + \langle\boldsymbol{u}'\cdot\boldsymbol{\mathcal{X}}'\rangle \\ &= -\langle\boldsymbol{u}'\cdot\nabla_{\mathrm{h}}\phi'\rangle - \left[\langle\boldsymbol{u}'\cdot(\boldsymbol{v}\cdot\nabla\boldsymbol{u})'\rangle - \langle\boldsymbol{u}'\boldsymbol{v}'\rangle\cdot\nabla\langle\boldsymbol{u}\rangle\right] - \langle\boldsymbol{u}'\boldsymbol{v}'\rangle\cdot\nabla\langle\boldsymbol{u}\rangle + \langle\boldsymbol{u}'\cdot\boldsymbol{\mathcal{X}}'\rangle\,. \end{aligned} \tag{A.11}$$

The spectral budget of EKE, therefore, becomes

$$\begin{aligned} \underbrace{\frac{1}{C_\Xi}\left\langle\tilde{\boldsymbol{u}}'^*\cdot\tilde{\boldsymbol{u}}'_t\right\rangle x_0^2 k}_{\mathcal{T}_K} = & \underbrace{-\frac{1}{C_\Xi}\left\langle\tilde{\boldsymbol{u}}'^*\cdot\widetilde{\nabla_{\mathrm{h}}\phi'}\right\rangle x_0^2 k}_{\mathcal{P}_K} \\ & \underbrace{-\frac{1}{C_\Xi}\left[\left\langle\tilde{u}'^*\widetilde{(\boldsymbol{v}\cdot\nabla u)'}\right\rangle + \left\langle\tilde{v}'^*\widetilde{(\boldsymbol{v}\cdot\nabla v)'}\right\rangle - \left\langle\tilde{u}'^*\widetilde{\boldsymbol{v}'\cdot\nabla\langle u\rangle}\right\rangle - \left\langle\tilde{v}'^*\widetilde{\boldsymbol{v}'\cdot\nabla\langle v\rangle}\right\rangle\right] x_0^2 k}_{\mathcal{A}_K} \\ & \underbrace{-\frac{1}{C_\Xi}\left[\left\langle\tilde{u}'^*\widetilde{\boldsymbol{v}'\cdot\nabla\langle u\rangle}\right\rangle - \left\langle\tilde{v}'^*\widetilde{\boldsymbol{v}'\cdot\nabla\langle v\rangle}\right\rangle\right] x_0^2 k}_{\mathrm{MtE}_K} + \underbrace{\frac{1}{C_\Xi}\left\langle\tilde{\boldsymbol{u}}'^*\cdot\widetilde{\boldsymbol{\mathcal{X}}'}\right\rangle x_0^2 k}_{\mathcal{D}_K}\,, \end{aligned} \tag{A.12}$$

(cf. (11)) where $\mathcal{A}_K$ is equivalent to $-\frac{1}{C_\Xi}\left[\left\langle \tilde{u'}^{*}\widetilde{(\boldsymbol{v}\cdot\nabla u')}\right\rangle + \left\langle \tilde{v'}^{*}\widetilde{(\boldsymbol{v}\cdot\nabla v')}\right\rangle\right] x_0^2 k$, and MtE$_K$ is the KE exchange between the mean and eddy flow.

References

Abernathey, R.P., Busecke, J., Smith, T., Banihirwe, A., Fernandes, F., Bourbeau, J., Cherian, D., Dussin, R., Swanson-Hysell, N., Constantinou, N., Ponte, A., et al., 2021. `xgcm`: General Circulation Model Postprocessing with xarray [Software]. Zenodo. URL: `https://xgcm.readthedocs.io/en/latest/`, doi:`10.5281/zenodo.3634752`.

Abernathey, R.P., et al., 2022. `xmitgcm`: Read MITgcm mds binary files into xarray [Software]. Zenodo. URL: `https://github.com/MITgcm/xmitgcm`, doi:`10.5281/zenodo.5139886`.

Ajayi, A., Le Sommer, J., Chassignet, E.P., Molines, J.M., Xu, X., Albert, A., Cosme, E., 2020. Spatial and temporal variability of the north atlantic eddy field from two kilometric-resolution ocean models. Journal of Geophysical Research: Oceans 125, e2019JC015827. doi:`10.1029/2019JC015827`.

Ajayi, A., Le Sommer, J., Chassignet, E.P., Molines, J.M., Xu, X., Albert, A., Dewar, W.K., 2021. Diagnosing cross-scale kinetic energy exchanges from two submesoscale permitting ocean models. Journal of Advances in Modeling Earth Systems doi:`10.1029/2019MS001923`.

Aluie, H., Hecht, M., Vallis, G., 2018. Mapping the energy cascade in the North Atlantic Ocean: The coarse-graining approach. Journal of Physical Oceanography 48, 225–244. doi:`10.1175/JPO-D-17-0100.1`.

Andres, M., Toole, J., Torres, D., Smethie Jr, W., Joyce, T., Curry, R., 2016. Stirring by deep cyclones and the evolution of Denmark Strait Overflow Water observed at Line W. Deep Sea Research Part I: Oceanographic Research Papers 109, 10–26. doi:`10.1016/j.dsr.2015.12.011`.

Aoki, K., 2014. A constraint on the thickness-weighted average equation of motion deduced from energetics. Journal of Marine Research 72, 355–382. doi:`10.1357/002224014815469886`.

Arbic, B.K., Polzin, K.L., Scott, R.B., Richman, J.G., Shriver, J.F., 2013. On eddy viscosity, energy cascades, and the horizontal resolution of gridded satellite altimeter products. Journal of Physical Oceanography 43, 283–300. doi:`10.1175/JPO-D-11-0240.1`.

Balwada, D., LaCasce, J.H., Speer, K.G., 2016. Scale-dependent distribution of kinetic energy from surface drifters in the Gulf of Mexico. Geophysical Research Letters 43, 10–856. doi:`10.1002/2016GL069405`.

Balwada, D., Xie, J.H., Marino, R., Feraco, F., 2022. Direct observational evidence of an oceanic dual kinetic energy cascade and its seasonality. Science Advances doi:10.1126/sciadv.abq2566.

Barkan, R., Srinivasan, K., Yang, L., McWilliams, J.C., Gula, J., Vic, C., 2021. Oceanic mesoscale eddy depletion catalyzed by internal waves. Geophysical Research Letters 48, e2021GL094376. doi:10.1029/2021GL094376.

Beech, N., Rackow, T., Semmler, T., Danilov, S., Wang, Q., Jung, T., 2022. Long-term evolution of ocean eddy activity in a warming world. Nature climate change 12, 910–917. doi:10.1038/s41558-022-01478-3.

Berloff, P., Ryzhov, E., Shevchenko, I., 2021. On dynamically unresolved oceanic mesoscale motions. Journal of Fluid Mechanics doi:10.1017/jfm.2021.477.

Boccaletti, G., Ferrari, R., Fox-Kemper, B., 2007. Mixed layer instabilities and restratification. Journal of Physical Oceanography 37, 2228–2250.

Buzzicotti, M., Storer, B., Khatri, H., Griffies, S., Aluie, H., 2023. Spatio-temporal coarse-graining decomposition of the global ocean geostrophic kinetic energy. Journal of Advances in Modeling Earth Systems 15, e2023MS003693.

Callies, J., Ferrari, R., 2013. Interpreting energy and tracer spectra of upper-ocean turbulence in the submesoscale range (1–200 km). Journal of Physical Oceanography 43, 2456–2474. doi:10.1175/JPO-D-13-063.1.

Campagne, A., Gallet, B., Moisy, F., Cortet, P.P., 2014. Direct and inverse energy cascades in a forced rotating turbulence experiment. Physics of Fluids 26, 125112. doi:10.1063/1.4904957.

Capet, X., McWilliams, J.C., Molemaker, M.J., Shchepetkin, A.F., 2008. Mesoscale to submesoscale transition in the california current system. Part I: Flow structure, eddy flux, and observational tests. Journal of Physical Oceanography 38, 29–43. doi:10.1175/2007JPO3671.1.

Charney, J.G., 1971. Geostrophic turbulence. Journal of the Atmospheric Sciences 28, 1087–1095. doi:10.1175/1520-0469(1971)028<1087:GT>2.0.CO;2.

Chassignet, E.P., Marshall, D.P., 2008. Gulf Stream separation in numerical ocean models. Geophysical Monograph Series 177. doi:10.1029/177GM05.

Chassignet, E.P., Xu, X., 2017. Impact of horizontal resolution (1/12°to 1/50°) on Gulf Stream separation, penetration, and variability. Journal of Physical Oceanography 47, 1999–2021. doi:10.1175/JPO-D-17-0031.1.

Chassignet, E.P., Xu, X., Bozec, A., Uchida, T., 2023. Impact of the New England seamount chain on Gulf Stream pathway and variability. Journal of Physical Oceanography doi:10.1175/JPO-D-23-0008.1.

Chassignet, E.P., Yeager, S.G., Fox-Kemper, B., Bozec, A., Castruccio, F., Danabasoglu, G., Horvat, C., Kim, W.M., Koldunov, N., Li, Y., et al., 2020. Impact of horizontal resolution on global ocean–sea ice model simulations based on the experimental protocols of the Ocean Model Intercomparison Project phase 2 (OMIP-2). Geoscientific Model Development 13, 4595–4637. doi:10.5194/gmd-13-4595-2020.

Chen, R., Flierl, G.R., 2015. The contribution of striations to the eddy energy budget and mixing: Diagnostic frameworks and results in a quasigeostrophic barotropic system with mean flow. Journal of Physical Oceanography 45, 2095–2113. doi:10.1175/JPO-D-14-0199.1.

Constantinou, N.C., Hogg, A.M., 2021. Intrinsic oceanic decadal variability of upper-ocean heat content. Journal of Climate , 1–42doi:10.1175/JCLI-D-20-0962.1.

Contreras, M., Renault, L., Marchesiello, P., 2023. Understanding energy pathways in the Gulf Stream. Journal of Physical Oceanography 53, 719–736. doi:10.1175/JPO-D-22-0146.1.

Danilov, S., Gurarie, D., 2004. Scaling, spectra and zonal jets in beta-plane turbulence. Physics of fluids 16, 2592–2603.

Daubechies, I., 1992. Ten lectures on wavelets. SIAM.

Deremble, B., Uchida, T., Dewar, W.K., Samelson, R.M., 2023. Eddy-mean flow interaction with a multiple scale quasi geostrophic model. Journal of Advances in Modeling Earth Systems doi:10.1029/2022MS003572.

Dewar, W.K., Parfitt, R., Wienders, N., 2022. Routine reversal of the AMOC in an ocean model ensemble. Geophysical Research Letters , e2022GL100117doi:10.1029/2022GL100117.

Gabor, D., 1946. Theory of communication. Part 1: The analysis of information. Journal of the Institution of Electrical Engineers-Part III: Radio and Communication Engineering 93, 429–441.

Gage, K.S., Nastrom, G.D., 1986. Theoretical interpretation of atmospheric wavenumber spectra of wind and temperature observed by commercial aircraft during GASP. Journal of Atmospheric Sciences 43, 729–740. doi:10.1175/1520-0469(1986)043<0729:TIOAWS>2.0.CO;2.

Galperin, B., Nakano, H., Huang, H.P., Sukoriansky, S., 2004. The ubiquitous zonal jets in the atmospheres of giant planets and Earth's oceans. Geophysical research letters 31.

Galperin, B., Sukoriansky, S., Dikovskaya, N., Read, P., Yamazaki, Y., Wordsworth, R., 2006. Anisotropic turbulence and zonal jets in rotating flows with a β-effect. Nonlinear Processes in Geophysics 13, 83–98.

Gent, P.R., 2011. The Gent–McWilliams parameterization: 20/20 hindsight. Ocean Modelling 39, 2–9. doi:10.1016/j.ocemod.2010.08.002.

Gent, P.R., McWilliams, J.C., 1990. Isopycnal mixing in ocean circulation models. Journal of Physical Oceanography 20, 150–155. doi:10.1175/1520-0485(1990)020<0150:IMIOCM>2.0.CO;2.

Germe, A., Hirschi, J.J.M., Blaker, A.T., Sinha, B., 2022. Chaotic variability of the atlantic meridional overturning circulation at subannual time scales. Journal of Physical Oceanography 52, 929–949. doi:10.1175/JPO-D-21-0100.1.

Griffies, S.M., Winton, M., Anderson, W.G., Benson, R., Delworth, T.L., Dufour, C.O., Dunne, J.P., Goddard, P., Morrison, A.K., Rosati, A., et al., 2015. Impacts on ocean heat from transient mesoscale eddies in a hierarchy of climate models. Journal of Climate 28, 952–977. doi:10.1175/JCLI-D-14-00353.1.

Grooms, I., Julien, K., Fox-Kemper, B., 2011. On the interactions between planetary geostrophy and mesoscale eddies. Dynamics of atmospheres and oceans 51, 109–136. doi:10.1016/j.dynatmoce.2011.02.002.

Guillaumin, A.P., Zanna, L., 2021. Stochastic-deep learning parameterization of ocean momentum forcing. Journal of Advances in Modeling Earth Systems 13, e2021MS002534. doi:10.1029/2021MS002534.

Held, I.M., Pierrehumbert, R.T., Garner, S.T., Swanson, K.L., 1995. Surface quasi-geostrophic dynamics. Journal of Fluid Mechanics 282, 1–20. doi:10.1017/S0022112095000012.

Jamet, Q., Ajayi, A., Le Sommer, J., Penduff, T., Hogg, A., Dewar, W.K., 2020a. On energy cascades in general flows: A Lagrangian application. Journal of Advances in Modeling Earth Systems 12, e2020MS002090. doi:10.1029/2020MS002090.

Jamet, Q., Deremble, B., Wienders, N., Uchida, T., Dewar, W.K., 2020b. On wind-driven energetics of subtropical gyres. Journal of Advances in Modeling Earth Systems 13, e2020MS002329. doi:10.1029/2020MS002329.

Jamet, Q., Dewar, W.K., Wienders, N., Deremble, B., 2019a. Fast warming of the surface ocean under a climatological scenario. Geophysical Research Letters 46, 3871–3879. doi:10.1029/2019GL082336.

Jamet, Q., Dewar, W.K., Wienders, N., Deremble, B., 2019b. Spatio-temporal patterns of chaos in the Atlantic Overturning Circulation. Geophysical Research Letters doi:10.1029/2019GL082552.

Jamet, Q., Dewar, W.K., Wienders, N., Deremble, B., Close, S., Penduff, T., 2020c. Locally and remotely forced subtropical AMOC variability: A matter of time scales. Journal of Climate 33, 5155–5172. doi:10.1175/JCLI-D-19-0844.1.

Jamet, Q., Leroux, S., Dewar, W.K., Penduff, T., Le Sommer, J., Molines, J.M., Gula, J., 2022. Non-local eddy-mean kinetic energy transfers in submesoscale-permitting ensemble simulations. Journal of Advances in Modeling Earth Systems doi:10.1029/2022MS003057.

Jansen, M.F., Adcroft, A., Khani, S., Kong, H., 2019. Toward an energetically consistent, resolution aware parameterization of ocean mesoscale eddies. Journal of Advances in Modeling Earth Systems 11, 2844–2860. doi:10.1029/2019MS001750.

Kay, J.E., Deser, C., Phillips, A., Mai, A., Hannay, C., Strand, G., Arblaster, J.M., Bates, S., Danabasoglu, G., Edwards, J., et al., 2015. The Community Earth System Model (CESM) large ensemble project: A community resource for studying climate change in the presence of internal climate variability. Bulletin of the American Meteorological Society 96, 1333–1349. doi:10.1175/BAMS-D-13-00255.1.

Khatri, H., Griffies, S.M., Uchida, T., Wang, H., Menemenlis, D., 2021. Role of mixed-layer instabilities in the seasonal evolution of eddy kinetic energy spectra in a global submesoscale permitting simulation. Geophysical Research Letters 48, e2021GL094777. doi:10.1029/2021GL094777.

Khatri, H., Sukhatme, J., Kumar, A., Verma, M.K., 2018. Surface ocean enstrophy, kinetic energy fluxes, and spectra from satellite altimetry. Journal of Geophysical Research: Oceans 123, 3875–3892. doi:10.1029/2017JC013516.

LaCasce, J., 2016. Estimating eulerian energy spectra from drifters. Fluids 1, 33. doi:10.3390/fluids1040033.

Lapeyre, G., 2017. Surface quasi-geostrophy. Fluids 2, 7. doi:10.3390/fluids2010007.

Large, W., McWilliams, J., Doney, S., 1994. Oceanic vertical mixing: A review and a model with a nonlocal boundary layer parameterization. Reviews of Geophysics 32, 363–403.

Leroux, S., Brankart, J.M., Albert, A., Brodeau, L., Molines, J.M., Jamet, Q., Le Sommer, J., Penduff, T., Brasseur, P., 2022. Ensemble quantification of short-term predictability of the ocean dynamics at a kilometric-scale resolution: a Western Mediterranean test case. Ocean Science 18, 1619–1644. doi:10.5194/os-18-1619-2022.

Leroux, S., Penduff, T., Bessières, L., Molines, J.M., Brankart, J.M., Sérazin, G., Barnier, B., Terray, L., 2018. Intrinsic and atmospherically forced variability of the AMOC: Insights from a large-ensemble ocean hindcast. Journal of Climate 31, 1183–1203. doi:10.1175/JCLI-D-17-0168.1.

Li, L., Deremble, B., Lahaye, N., Mémin, E., 2023. Stochastic data-driven parameterization of unresolved eddy effects in a baroclinic quasi-geostrophic model. Journal of Advances in Modeling Earth Systems 15, e2022MS003297. doi:10.1029/2022MS003297.

Lindborg, E., 2015. A Helmholtz decomposition of structure functions and spectra calculated from aircraft data. Journal of Fluid Mechanics 762. doi:10.1017/jfm.2014.685.

Liu, L., Yu, X., Xue, H., Xiu, P., 2023. Reconstructability of Open-Ocean Upper-Layer Dynamics From Surface Observations Using Surface Quasigeostrophy (SQG) Theory. Journal of Geophysical Research: Oceans 128, e2023JC020124.

Loose, N., Bachman, S., Grooms, I., Jansen, M., 2022. Diagnosing scale-dependent energy cycles in a high-resolution isopycnal ocean model. Journal of Physical Oceanography 53, 157–176. doi:10.1175/JPO-D-22-0083.1.

Lorenz, E.N., 1963. Deterministic nonperiodic flow. Journal of atmospheric sciences 20, 130–141. doi:10.1175/1520-0469(1963)020<0130:DNF>2.0.CO;2.

Maddison, J.R., Marshall, D.P., 2013. The Eliassen–Palm flux tensor. Journal of Fluid Mechanics 729, 69–102. doi:10.1017/jfm.2013.259.

Maher, N., Milinski, S., Suarez-Gutierrez, L., Botzet, M., Dobrynin, M., Kornblueh, L., Kröger, J., Takano, Y., Ghosh, R., Hedemann, C., et al., 2019. The Max Planck Institute Grand Ensemble: Enabling the exploration of climate system variability. Journal of Advances in Modeling Earth Systems 11, 2050–2069. doi:10.1029/2019MS001639.

Marshall, D., Maddison, J., Berloff, P., 2012. A framework for parameterizing eddy potential vorticity fluxes. Journal of Physical Oceanography 42, 539–557.

Maximenko, N.A., Bang, B., Sasaki, H., 2005. Observational evidence of alternating zonal jets in the world ocean. Geophysical research letters 32.

Meunier, J., Miquel, B., Gallet, B., 2023. A direct derivation of the Gent–McWilliams/Redi diffusion tensor from quasi-geostrophic dynamics. Journal of Fluid Mechanics 963, A22. doi:10.1017/jfm.2023.347.

Miracca-Lage, M., González-Haro, C., Napolitano, D.C., Isern-Fontanet, J., Polito, P.S., 2022. Can the Surface Quasi-Geostrophic (SQG) Theory Explain Upper Ocean Dynamics in the South Atlantic? Journal of Geophysical Research: Oceans 127, e2021JC018001.

Morlet, J., Arens, G., Fourgeau, E., Glard, D., 1982. Wave propagation and sampling theory—Part I: Complex signal and scattering in multilayered media. Geophysics 47, 203–221. doi:10.1190/1.1441328.

Özgökmen, T.M., Poje, A.C., Fischer, P.F., Haza, A.C., 2011. Large eddy simulations of mixed layer instabilities and sampling strategies. Ocean Modelling 39, 311–331.

Pearson, J., Fox-Kemper, B., Pearson, B., Chang, H., Haus, B.K., Horstmann, J., Huntley, H.S., Kirwan Jr, A., Lund, B., Poje, A., 2020. Biases in structure functions from observations of submesoscale flows. Journal of Geophysical Research: Oceans 125, e2019JC015769. doi:10.1029/2019JC015769.

Pedlosky, J., et al., 1987. Geophysical fluid dynamics. volume 710. Springer.

Perrier, V., Philipovitch, T., Basdevant, C., 1995. Wavelet spectra compared to Fourier spectra. Journal of mathematical physics 36, 1506–1519. doi:10.1063/1.531340.

Poincaré, H., 1890. On the three-body problem and the equations of dynamics. Acta Math 13.

Poje, A.C., Özgökmen, T.M., Bogucki, D.J., Kirwan, A., 2017. Evidence of a forward energy cascade and kolmogorov self-similarity in submesoscale ocean surface drifter observations. Physics of Fluids 29, 020701. doi:10.1063/1.4974331.

Redi, M.H., 1982. Oceanic isopycnal mixing by coordinate rotation. Journal of Physical Oceanography 12, 1154–1158. doi:10.1175/1520-0485(1982)012<1154:OIMBCR>2.0.CO;2.

Renault, L., Molemaker, M.J., Gula, J., Masson, S., McWilliams, J.C., 2016. Control and stabilization of the gulf stream by oceanic current interaction with the atmosphere. Journal of Physical Oceanography 46, 3439–3453. doi:10.1175/JPO-D-16-0115.1.

Rocha, C.B., Chereskin, T.K., Gille, S.T., Menemenlis, D., 2016. Mesoscale to submesoscale wavenumber spectra in Drake Passage. Journal of Physical Oceanography 46, 601–620. doi:10.1175/JPO-D-15-0087.1.

Romanou, A., Rind, D., Jonas, J., Miller, R., Kelley, M., Russell, G., Orbe, C., Nazarenko, L., Latto, R., Schmidt, G.A., 2023. Stochastic bifurcation of the North Atlantic Circulation under a mid-range future climate scenario with the NASA-GISS modelE. Journal of Climate , 1–49doi:10.1175/JCLI-D-22-0536.1.

Saba, V.S., Griffies, S.M., Anderson, W.G., Winton, M., Alexander, M.A., Delworth, T.L., Hare, J.A., Harrison, M.J., Rosati, A., Vecchi, G.A., et al., 2016. Enhanced warming of the Northwest Atlantic Ocean under climate change. Journal of Geophysical Research: Oceans 121, 118–132. doi:10.1002/2015JC011346.

Sadek, M., Aluie, H., 2018. Extracting the spectrum of a flow by spatial filtering. Physical Review Fluids 3, 124610. doi:10.1103/PhysRevFluids.3.124610.

Schubert, R., Gula, J., Greatbatch, R.J., Baschek, B., Biastoch, A., 2020. The submesoscale kinetic energy cascade: Mesoscale absorption of submesoscale mixed layer eddies and frontal downscale fluxes. Journal of Physical Oceanography 50, 2573–2589. doi:10.1175/JPO-D-19-0311.1.

Scott, R., Wang, F., 2005. Direct evidence of an oceanic inverse kinetic energy cascade from satellite altimetry. Journal of Physical Oceanography 35, 1650–1666. doi:10.1175/JPO2771.1.

Sérazin, G., Jaymond, A., Leroux, S., Penduff, T., Bessières, L., Llovel, W., Barnier, B., Molines, J.M., Terray, L., 2017. A global probabilistic study of the ocean heat content low-frequency variability: Atmospheric forcing versus oceanic chaos. Geophysical Research Letters 44, 5580–5589. doi:10.1002/2017GL073026.

Srinivasan, K., Barkan, R., McWilliams, J.C., 2022. A forward energy flux at submesoscales driven by frontogenesis. Journal of Physical Oceanography doi:10.1175/JPO-D-22-0001.1.

Stainforth, D.A., Allen, M.R., Tredger, E.R., Smith, L.A., 2007. Confidence, uncertainty and decision-support relevance in climate predictions. Philosophical Transactions of the Royal Society A: Mathematical, Physical and Engineering Sciences 365, 2145–2161. doi:10.1098/rsta.2007.2074.

Stammer, D., 1998. On eddy characteristics, eddy transports, and mean flow properties. Journal of Physical Oceanography 28, 727–739. doi:10.1175/1520-0485(1998)028<0727:OECETA>2.0.CO;2.

Stammer, D., Wunsch, C., 1999. Temporal changes in eddy energy of the oceans. Deep Sea Research Part II: Topical Studies in Oceanography 46, 77–108. doi:10.1016/S0967-0645(98)00106-4.

Steinberg, J.M., Eriksen, C.C., 2022. Eddy Vertical Structure and Variability: Deepglider Observations in the North Atlantic. Journal of Physical Oceanography 52, 1091–1110.

Storer, B.A., Buzzicotti, M., Khatri, H., Griffies, S.M., Aluie, H., 2022. Global energy spectrum of the general oceanic circulation. Nature communications 13, 1–9. doi:s41467-022-33031-3.

Storer, B.A., Buzzicotti, M., Khatri, H., Griffies, S.M., Aluie, H., 2023. Global cascade of kinetic energy in the ocean and the atmospheric imprint. Science Advances 9, eadi7420.

Tedesco, P., Baker, L., Naveira Garabato, A., Mazloff, M., Gille, S., Caulfield, C., Mashayek, A., 2023. Spatiotemporal characteristics of the near-surface turbulent cascade at the submesoscale in the drake passage. Journal of Physical Oceanography .

Uchida, T., Abernathey, R.P., Smith, K.S., 2017. Seasonality of eddy kinetic energy in an eddy permitting global climate model. Ocean Modelling 118, 41–58. doi:10.1016/j.ocemod.2017.08.006.

Uchida, T., Balwada, D., Abernathey, R.P., McKinley, G.A., Smith, K.S., Lévy, M., 2019. The contribution of submesoscale over mesoscale eddy iron transport in the open Southern Ocean. Journal of Advances in Modeling Earth Systems 11, 3934–3958. doi:10.1029/2019MS001805.

Uchida, T., Balwada, D., Abernathey, R.P., McKinley, G.A., Smith, K.S., Lévy, M., 2020. Vertical eddy iron fluxes support primary production in the open Southern Ocean. Nature Communications 11, 1125. doi:10.1038/s41467-020-14955-0.

Uchida, T., Balwada, D., Jamet, Q., Dewar, W.K., Deremble, B., Penduff, T., Le Sommer, J., 2023a. Cautionary tales from the mesoscale eddy transport tensor. Ocean Modelling 182, 102172. doi:10.1016/j.ocemod.2023.102172.

Uchida, T., Deremble, B., Dewar, W.K., Penduff, T., 2021a. Diagnosing the Eliassen-Palm flux from a quasi-geostrophic double gyre ensemble, in: EarthCube Annual Meeting, NSF. URL: https://earthcube2021.github.io/ec21_book/notebooks/ec21_uchida_etal/notebooks/TU_05_Diagnosing-the-Eliassen-Palm-flux-from-a-quasi-geostrophic-double-gyre-ensemble.html, doi:10.5281/zenodo.5496375.

Uchida, T., Deremble, B., Penduff, T., 2021b. The seasonal variability of the ocean energy cycle from a quasi-geostrophic double gyre ensemble. Fluids 6, 206. doi:10.3390/fluids6060206.

Uchida, T., Deremble, B., Popinet, S., 2022a. Deterministic model of the eddy dynamics for a midlatitude ocean model. Journal of Physical Oceanography 52, 1133–1154. doi:10.1175/JPO-D-21-0217.1.

Uchida, T., Dewar, W.K., 2022. xwavelet: Wavelet transforms for xarray data [Software]. Zenodo. URL: https://github.com/roxyboy/xwavelet/tree/v1.0.0, doi:10.5281/zenodo.6022738.

Uchida, T., Jamet, Q., Dewar, W.K., Balwada, D., Le Sommer, J., Penduff, T., 2022b. Diagnosing the thickness-weighted averaged eddy-mean flow interaction in an eddying North Atlantic ensemble: The Eliassen–Palm flux. Journal of Advances in Modeling Earth Systems 14, e2021MS002866. doi:10.1029/2021MS002866.

Uchida, T., Jamet, Q., Dewar, W.K., Deremble, B., Poje, A.C., Sun, L., 2024. Imprint of chaos on the ocean energy cycle from an eddying North Atlantic ensemble. Journal of Physical Oceanography doi:10.1175/JPO-D-23-0176.1.

Uchida, T., Jamet, Q., Poje, A.C., Dewar, W.K., 2021c. An ensemble-based eddy and spectral analysis, with application to the Gulf Stream. Journal of Advances in Modeling Earth Systems 14, e2021MS002692. doi:10.1029/2021MS002692.

Uchida, T., Jamet, Q., Poje, A.C., Wienders, N., Dewar, W.K., Deremble, B., 2023b. Wavelet-based wavenumber spectral estimate of eddy kinetic energy: Idealized quasi-geostrophic flow. Journal of Advances in Modeling Earth Systems 15, e2022MS003399. doi:10.1029/2022MS003399.

Uchida, T., Le Sommer, J., Stern, C., Abernathey, R.P., Holdgraf, C., Albert, A., Brodeau, L., Chassignet, E.P., Xu, X., Gula, J., et al., 2022c. Cloud-based framework for intercomparing submesoscale-permitting realistic ocean models. Geoscientific Model Development 15, 5829–5856. doi:10.5194/gmd-15-5829-2022.

Uchida, T., Rokem, A., Squire, D., Nicholas, T., Abernathey, R.P., Soler, S., Nouguier, F., Vanderplas, J., Paige, M., Mondal, A., Mayer, A., Halchenko, Y., Wilson, G., Constantinou, N., Ponte, A., Squire, D., Busecke, J., Spring, A., Pak, K., Scott, R., Hoyer, S., Moon, Z., et al., 2021d. `xrft`: Fourier transforms for xarray data [Software]. Zenodo. URL: https://xrft.readthedocs.io/en/latest/, doi:10.5281/zenodo.1402635.

Vallis, G., 2006. Atmospheric and Oceanic Fluid Dynamics. Cambridge.

Vergara, O., Morrow, R., Pujol, I., Dibarboure, G., Ubelmann, C., 2019. Revised global wavenumber spectra from recent altimeter observations. Journal of Geophysical Research: Oceans 124, 3523–3537. doi:10.1029/2018JC014844.

Waterman, S., Lilly, J.M., 2015. Geometric decomposition of eddy feedbacks in barotropic systems. Journal of Physical Oceanography 45, 1009–1024. doi:10.1175/JPO-D-14-0177.1.

Wunsch, C., 1981. The Evolution of Physical Oceanography: Scientific Surveys in Honor of Henry Stommel. MIT Press. chapter Low frequency variability of the sea. pp. 342–374.

Xu, G., Chang, P., Ramachandran, S., Danabasoglu, G., Yeager, S., Small, J., Zhang, Q., Jing, Z., Wu, L., 2022. Impacts of model horizontal resolution on mean sea-surface temperature biases in the community earth system model. Journal of Geophysical Research: Oceans , e2022JC019065doi:10.1029/2022JC019065.

Xu, Y., Fu, L.L., 2011. Global variability of the wavenumber spectrum of oceanic mesoscale turbulence. Journal of Physical Oceanography 41, 802–809. doi:https://doi.org/10.1175/2010JPO4558.1.

Xu, Y., Fu, L.L., 2012. The effects of altimeter instrument noise on the estimation of the wavenumber spectrum of sea surface height. Journal of Physical Oceanography 42, 2229–2233. doi:10.1175/JPO-D-12-0106.1.

Yarom, E., Vardi, Y., Sharon, E., 2013. Experimental quantification of inverse energy cascade in deep rotating turbulence. Physics of Fluids 25, 085105. doi:10.1063/1.4817666.

Yassin, H., Griffies, S.M., 2022. Surface quasigeostrophic turbulence in variable stratification. Journal of Physical Oceanography 52, 2995–3013. doi:10.1175/JPO-D-22-0040.1.

Young, W., 2010. Dynamic Enthalpy, Conservative Temperature, and the Seawater Boussinesq Approximation. Journal of Physical Oceanography 40, 394–400. doi:10.1175/2009JPO4294.1.

Young, W., 2012. An exact thickness-weighted average formulation of the Boussinesq equations. Journal of Physical Oceanography 42, 692–707. doi:10.1175/JPO-D-11-0102.1.

Zhao, D., Betti, R., Aluie, H., 2022. Scale interactions and anisotropy in Rayleigh–Taylor turbulence. Journal of Fluid Mechanics 930, A29.

Zhao, M., Ponte, R.M., Penduff, T., Close, S., Llovel, W., Molines, J.M., 2021. Imprints of ocean chaotic intrinsic variability on bottom pressure and implications for data and model analyses. Geophysical Research Letters 48, e2021GL096341. doi:10.1029/2021GL096341.

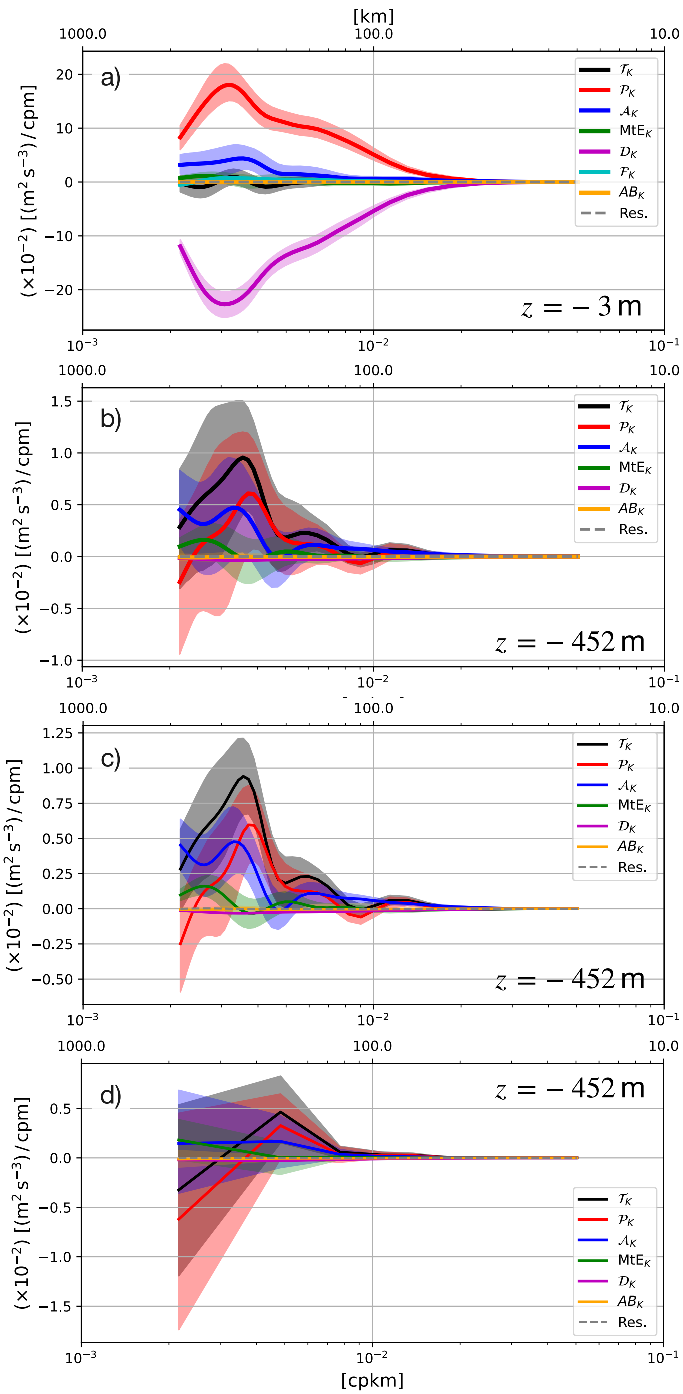

Figure 4: Isotropic EKE spectral budget (11) at the surface and below the mixed layer at location A. At the surface, there is an additional term due to wind stress $\mathcal{F}_K(k)$ (a). $\mathrm{AB}_K(k)$ stems from the Adam-Bashforth time stepping. Panel (b) exhibits the budget at location A at $z = -452\,\mathrm{m}$ while (c) exhibits it when averaged over neighboring nine grid points surrounding location A. Panel (d) shows the Fourier budget where land points are interpolated over and data are windowed prior to taking the FFT. The colored shadings indicate the 95% bootstrap confidence interval.

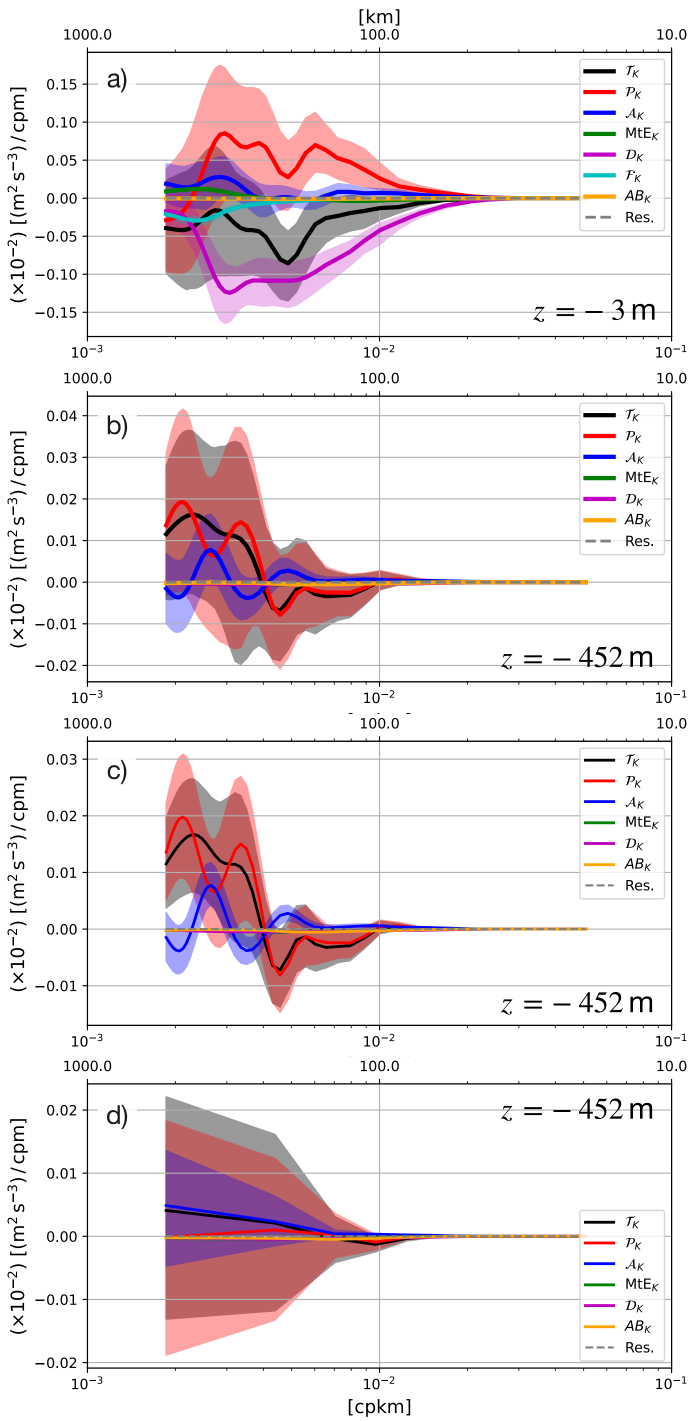

Figure 5: Same as Fig. 4 but for location B.

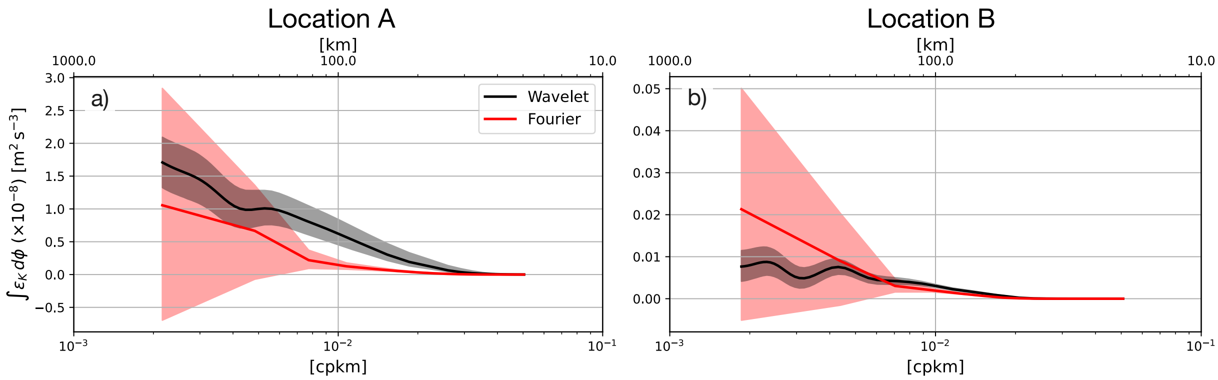

Figure 6: Isotropic EKE spectral flux $\varepsilon_K(k)$ at location A (a) and B (b) from $z = -452\,\mathrm{m}$ on January 1, 1967. The former is equivalent to $\mathcal{A}_K(k)$ in Fig. 4c, d integrated in wavenumber and latter in Fig. 5c, d. The wavelet approach is averaged over neighboring nine grid points. The FFT approach has the land cells interpolated over and is windowed while neither are applied for the wavelet approach. The colored shadings indicate the 95% bootstrap confidence interval.

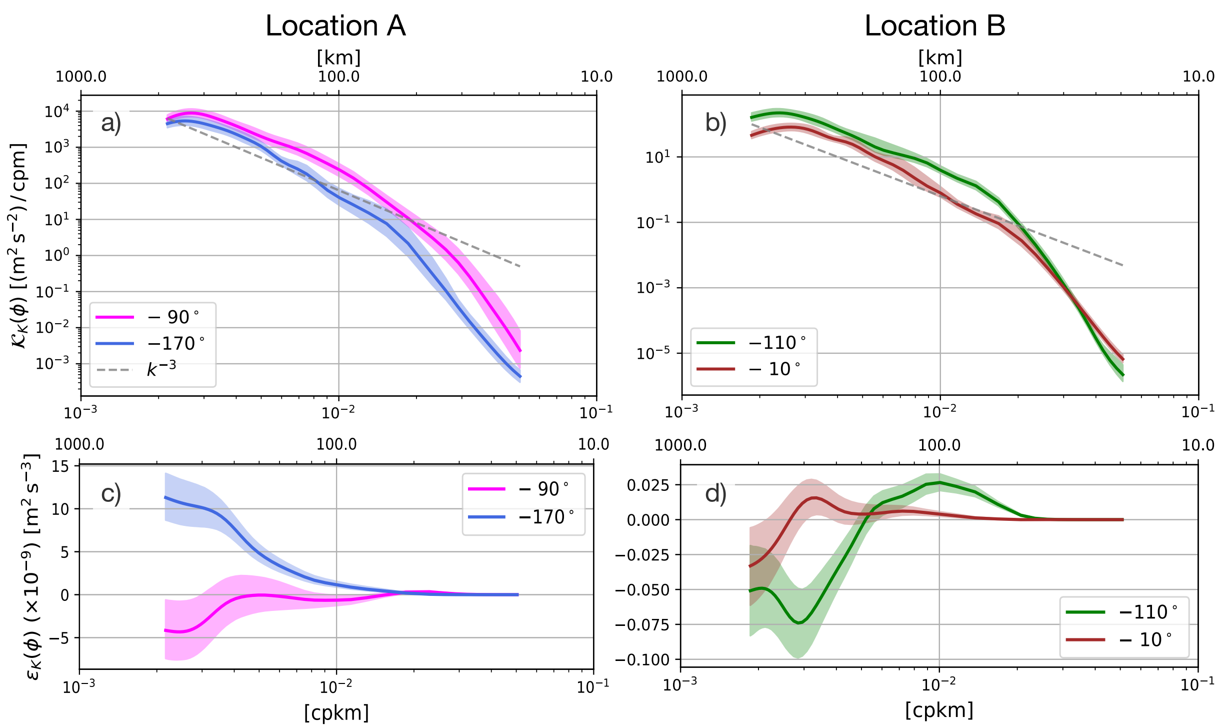

Figure 7: Wavelet-based EKE spectra $\mathscr{K}_K(\phi, k)$ plotted along the orientation of maximum and minimum energy from $z = -452\,\mathrm{m}$ at locations A (a) and B (b) on January 1, 1967. The angles, associated with the maximum and minimum energy at each location, are color coded. The 95% bootstrap confidence intervals are shown in colored shadings. Power law with the slope of -3 is indicated with the grey dashed line. The lower panels exhibit the EKE spectral flux $\varepsilon_K(\phi, k)$ oriented along the maximum and minimum energy about locations A (c) and B (d).

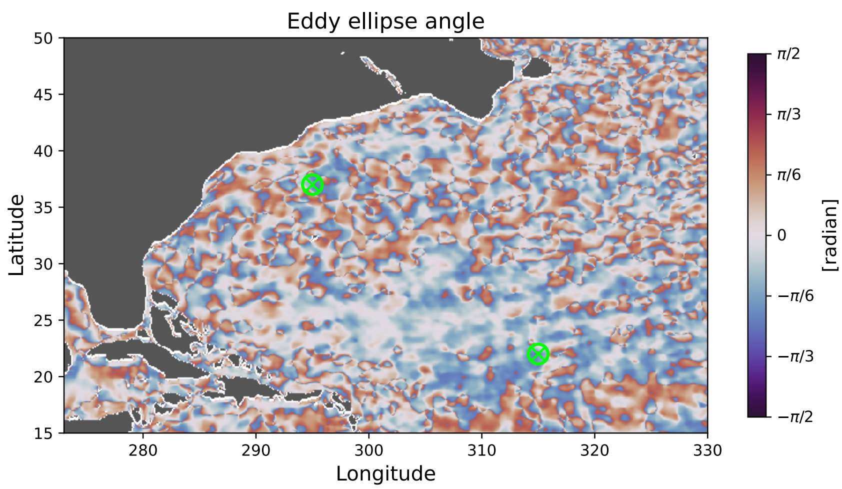

Figure 8: The eddy ellipse angle ϑ at $z = -452\,\mathrm{m}$ on January 1, 1967. The lime-colored markers $\otimes$ indicate locations A and B.

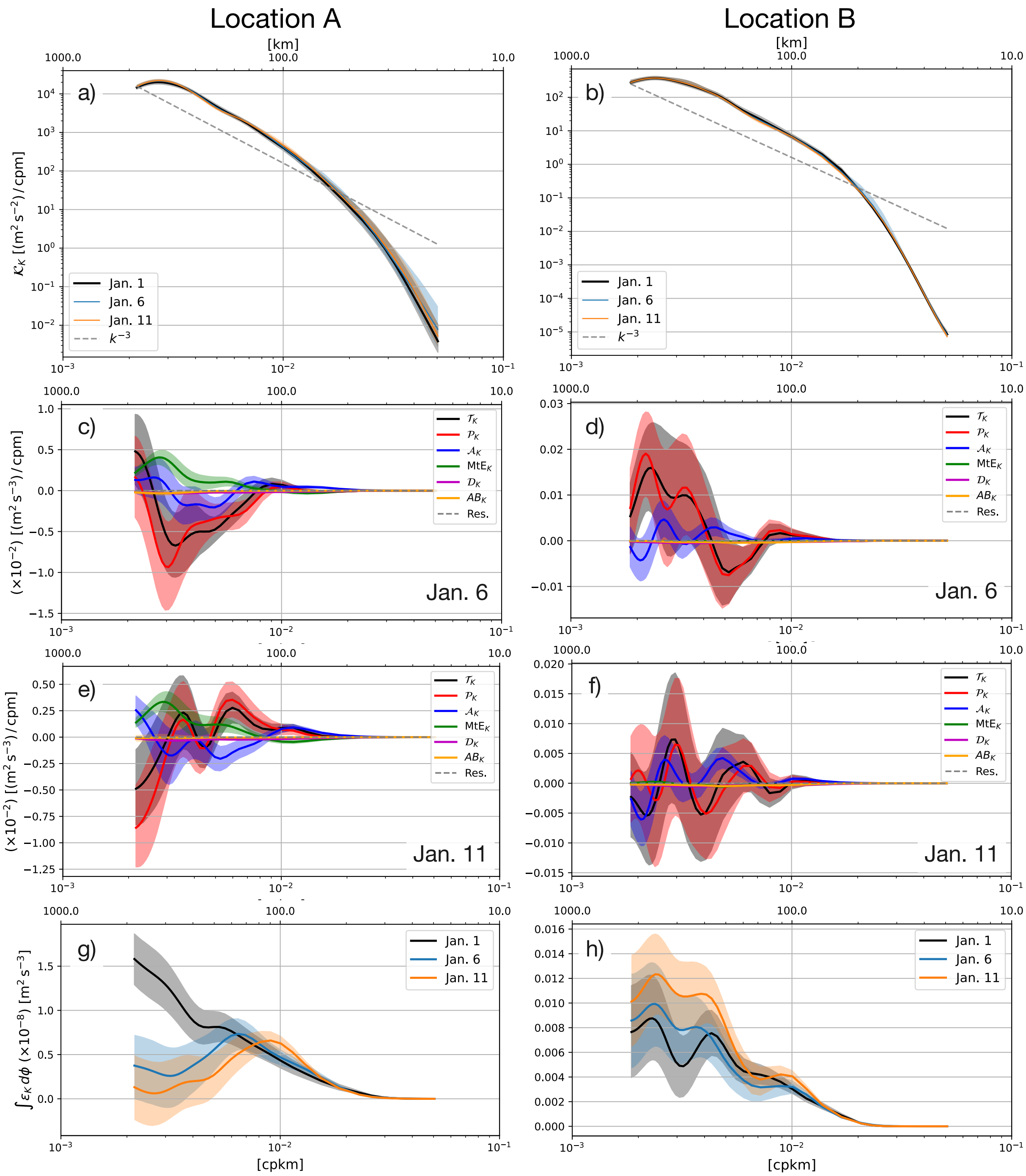

Figure 9: Isotropic wavelet-based spectra $\mathscr{K}_K(k)$ between January 1 – 11, 1967 from $z = -452\,\mathrm{m}$ at locations A and B (a, b). Isotropic wavelet-based spectral budget on January 6 and 11, 1967 from $z = -452\,\mathrm{m}$ (c - f). Isotropic wavelet-based spectral flux $\varepsilon_K(k)$ between January 1 – 11, 1967 from $z = -452\,\mathrm{m}$ (g, h). The spectra and spectral flux on January 1 are identical to those in Figs. 3 and 6 but are added here for comparison. The budgets and fluxes are averaged over nine neighboring points.

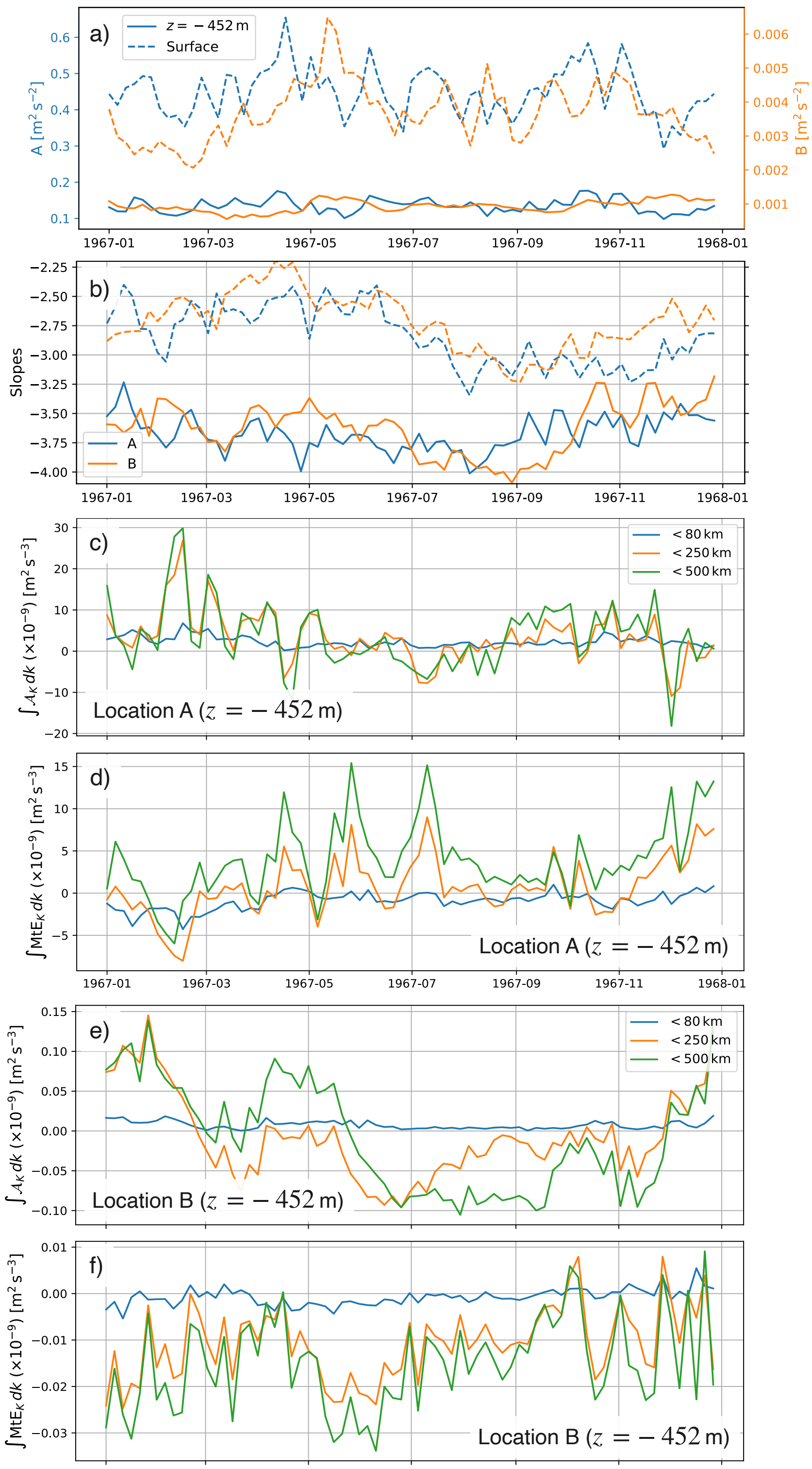

Figure 10: Time series of EKE at locations A and B (a) and of isotropic EKE spectral slopes at locations A and B (b). Dashed curves show the slopes at the surface while solid curves for $z = -452\,\mathrm{m}$. Location A is in blue and B in orange curves. The slopes were estimated by fitting a line to $\mathscr{K}_K(k)$ at scales between 250 - 80 km. EKE spectral transfer $\mathcal{A}_K(k)$ and shear production $\mathrm{MtE}_K(k)$ integrated over scales below 80 km, 250 km and 500 km are shown for location A (c, d) and B (e, f) at $z = -452\,\mathrm{m}$.

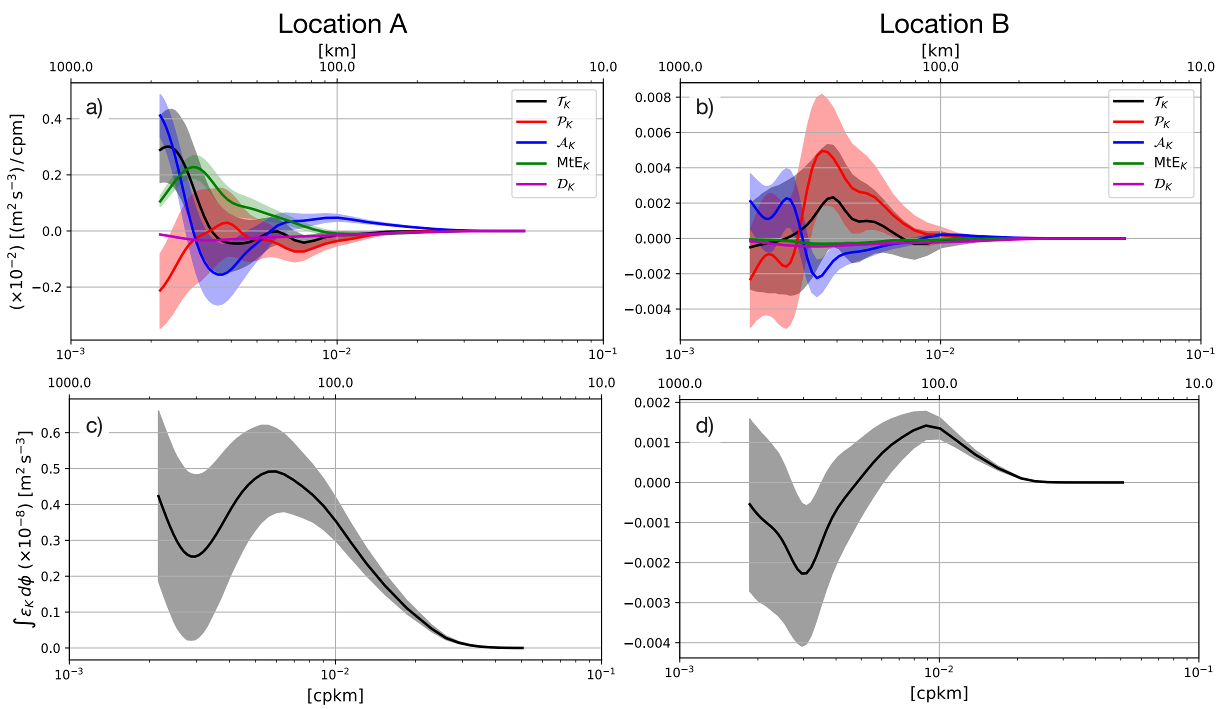

Figure 11: Annual mean of terms with significance in the ensemble-averaged wavelet-based spectral EKE budgets at location A (a) and B (b) at $z = -452\,\mathrm{m}$. The annual mean is taken after ensemble averaging the budgets every 15 days. Annual mean of EKE spectral flux $\varepsilon_K(k)$ at location A (c) and B (d).